Linear Stability Analysis of Transient Electrodeposition in Charged Porous Media: Suppression of Dendritic Growth by Surface Conduction

Edwin Khoo,[1,*] Hongbo Zhao,[1] and Martin Z. Bazant[1,2,*,z]

[1] *Department of Chemical Engineering, Massachusetts Institute of Technology, Cambridge, Massachusetts 02139, USA*
[2] *Department of Mathematics, Massachusetts Institute of Technology, Cambridge, Massachusetts 02139, USA*

We study the linear stability of transient electrodeposition in a charged random porous medium, whose pore surface charges can be of any sign, flanked by a pair of planar metal electrodes. Discretization of the linear stability problem results in a generalized eigenvalue problem for the dispersion relation that is solved numerically, which agrees well with the analytical approximation obtained from a boundary layer analysis valid at high wavenumbers. Under galvanostatic conditions in which an overlimiting current is applied, in the classical case of zero surface charges, the electric field at the cathode diverges at Sand's time due to electrolyte depletion. The same phenomenon happens for positive charges but earlier than Sand's time. However, negative charges allow the system to sustain an overlimiting current via surface conduction past Sand's time, keeping the electric field bounded. Therefore, at Sand's time, negative charges greatly reduce surface instabilities and suppress dendritic growth, while zero and positive charges magnify them. We compare theoretical predictions for overall surface stabilization with published experimental data for copper electrodeposition in cellulose nitrate membranes and demonstrate good agreement between theory and experiment. We also apply the stability analysis to how crystal grain size varies with duty cycle during pulse electroplating.

[DOI: 10.1149/2.1521910jes]

Manuscript submitted January 16, 2019; revised manuscript received May 23, 2019. Published June 28, 2019.

Linear stability analysis is routinely applied to nonlinear systems to study how the onset of instability is related to system parameters and to provide physical insights on the conditions and early dynamics of pattern formation.[1–3] Some examples in hydrodynamics include the Orr-Sommerfeld equation that predicts the dependence on Reynolds number of the transition from laminar flow to turbulent flow[4–7] and the electroconvective instability that causes the transition of a quasiequilibrium electric double layer to an nonequilibrium one that contains an additional extended space charge region.[8] Here, we focus on morphological stability analysis in which linear stability analysis is used to analyze morphological instabilities of interfaces formed between different phases observed in various diverse phenomena such as electrodeposition,[2,9–15] solidification[1–3,9] and morphogenesis.[3,16] Some particular examples of morphological stability analysis include the Saffman-Taylor instability (viscous fingering),[17–20] viscous fingering coupled with electrokinetic effects,[21] the Mullins-Sekerka instability of a spherical particle during diffusion-controlled or thermally controlled growth[22] and of a planar interface during solidification of a dilute binary alloy,[23,24] and control of phase separation using electro-autocatalysis or electro-autoinhibition in driven open electrochemical systems.[25,26]

Stability of metal electrodeposition.—We focus on electrodeposition as a specific example of an electrochemical system for which morphological stability has been widely researched both theoretically and experimentally. The fundamental aspect of electrodeposition concerns the inherent instability of the governing physics while the practical aspect is about applications such as electroplating of metals and charging of metal batteries. To elucidate the physics behind electrodeposition, in liquid electrolytes, the morphologies of electrodeposits formed and their transitions for metals such as copper, zinc and silver are particularly well studied.[9–13,15,27] Depending on conditions such as applied current, applied voltage and electrolyte concentration, a variety of morphological patterns such as diffusion-limited aggregation (DLA) patterns,[28–38] dense branching morphologies (DBM)[34–46] and dendritic structures[34–37,40,42,47–49] have been observed. Ion concentration fields,[50–55] electroconvection,[56–60] gravity-induced convection (buoyancy)[59–61] and the presence of impurities[44,62–65] have also been examined to determine their significant effects on morphology. While the range of possible morphologies of electrodeposits is diverse, for electroplating of metals, it is desirable to electrodeposit layers that are as uniform and homogeneous as possible.

Electrodeposition is also a critical process in the development of rechargeable/secondary lithium metal batteries (LMBs) that use lithium metal for the negative electrode. For negative electrodes that use lithium chemistry, because lithium metal has the lowest standard reduction potential ($-3.04\,\mathrm{V}$ vs. the standard hydrogen electrode), highest theoretical specific ($3860\,\mathrm{mAh/g}$) and volumetric ($2061\,\mathrm{mAh/cm^3}$) capacities, and lowest mass density ($0.53\,\mathrm{g/cm^3}$) out of all possible candidates, it is the most promising choice for achieving high energy densities in LMBs.[66–84] However, the charging of LMBs is equivalent to lithium electrodeposition at the negative electrode, which is an inherently unstable process that can cause the formation of dendrites that penetrate the separator and result in internal short circuits and thermal runaway during charging.[66–84] This process has been especially well investigated in lithium polymer batteries that use a polymer electrolyte.[85–92] Detailed studies of various growth modes of lithium in liquid electrolytes during charging have been recently performed,[93–95] which will aid in the development of better models for lithium electrodeposition. Modern lithium-ion batteries (LIBs)[66–73,75,79,84,96–99] partially mitigate this problem of dendrite formation and propagation by employing lithium intercalating materials such as graphite for the negative electrode where only lithium ions and not reduced lithium atoms are involved in the intercalation reactions, which is also known as the "rocking chair technology".[67] Nonetheless, lithium plating still occurs in LIBs when they are charged at high rates or low temperatures.[75,98–101] Although the root causes of the widely publicized LIB failures in two Boeing 787 Dreamliners in January 2013 were not conclusively identified,[102] there is no doubt that safety is of paramount importance in both LMBs and LIBs, which requires a thorough understanding of dendrite formation.

For both electroplating of metals and charging of high energy density LMBs, it would be advantageous to perform them at as large a current or voltage as possible without causing dendrite formation. It is therefore important to understand the possible mechanisms for the electrochemical system to sustain a high current or voltage and how these mechanisms interact with the metal electrodeposition and LMB charging processes. In a neutral channel or porous medium containing an electrolyte, when ion transport is governed by diffusion and electromigration, which is collectively termed electrodiffusion, the maximum current that can be attained by the electrochemical system is called the diffusion-limited current.[103,104] In practice, overlimiting

[*] Electrochemical Society Member.
[z] E-mail: bazant@mit.edu

current (OLC) beyond the electrodiffusion limit has been observed experimentally in ion-exchange membranes[105–116] and microchannels and nanochannels.[117–124] Depending on the length scale of the pores or channel, some possible physical mechanisms for OLC[125] are surface conduction,[119–121,126–128] electroosmotic flow[129,130] and electroosmotic instability.[8,131] Some chemical mechanisms for OLC include water splitting[114,115] and current-induced membrane discharge.[132] In this paper, we focus on porous media consisting of pores with a nanometer length scale, therefore the dominant OLC mechanism is expected to be surface conduction.[125] When a sufficiently large current or voltage is applied across a porous medium whose pore surfaces are charged, the bulk electrolyte eventually gets depleted at an ion-selective interface such as an electrode. In order to sustain the current beyond the electrodiffusion limit, the counterions in the electric double layers (EDLs) next to the charged pore surfaces migrate under the large electric field generated in the depletion region. This phenomenon is termed surface conduction and results in the formation and propagation of deionization shocks away from the ion-selective interface in porous media[127,128,133] and microchannels and nanochannels.[119–121,125,126,134] The deionization shock separates the "front" electrolyte-rich region, in which bulk electrodiffusion dominates, from the "back" electrolyte-poor region, in which electromigration in the EDLs dominates.

Theories of pattern formation.—Morphological stability analysis of electrodeposition is typically performed in the style of the pioneering Mullins-Sekerka stability analysis.[22,23] The destabilizing effect arises from the amplification of surface protrusions by diffusive fluxes while the main stabilizing effect arises from the surface energy penalty incurred in creating additional surface area. The balance between these two effects, which is influenced by system parameters, sets a characteristic length scale or wavenumber for the surface instability. In 1963, by applying an infinitesimally small spherical harmonic perturbation to the surface of a spherical particle undergoing growth by solute diffusion or heat diffusion, Mullins and Sekerka derived a dispersion relation that related growth rates of the eigenmodes to particle radius and degree of supersaturation.[22] Similarly, in 1964, Mullins and Sekerka imposed a infinitesimally small sinusoidal perturbation on a planar liquid-solid interface during the solidification of a dilute binary alloy and obtained a dispersion relation relating the surface perturbation growth rate to system parameters such as temperature and concentration gradients.[23] In the spirit of the Mullins-Sekerka stability analysis, about 16 years later in 1980, Aogaki, Kitazawa, Kose and Fueki applied linear stability analysis to study electrodeposition with a steady-state base state in the presence of a supporting electrolyte, i.e., electromigration of the minor species can be ignored, and without explicitly accounting for electrochemical reaction kinetics.[135] Following up on this work, from 1981 to 1982, Aogaki and Makino changed the steady-state base state to a time-dependent base state under galvanostatic conditions while keeping other assumptions intact.[136–138] In 1984, Aogaki and Makino extended their previous work to account for surface diffusion of adsorbed metal atoms under galvanostatic[139,140] and potentiostatic conditions.[141,142] In the same year, Makino, Aogaki and Niki also used such a linear stability analysis to extract surface parameters of metals under galvanostatic and potentiostatic conditions[143] and applied it to study how hydrogen adsorption affects these extracted parameters under galvanostatic conditions.[144] Later work by Barkey, Muller and Tobias in 1989,[145,146] and Chen and Jorne in 1991[147] additionally assumed the presence of a diffusion boundary layer next to the electrode.

Subsequent developments in linear stability analysis of electrodeposition relaxed some assumptions made in the past literature and added more physics and electrochemistry. Butler-Volmer reaction kinetics was first explicitly considered by Pritzker and Fahidy in 1992 for a steady-state base state with a diffusion boundary layer next to the electrode.[148] Also considering Butler-Volmer reaction kinetics with a steady-state base state, in 1995, Sundström and Bark used the Nernst-Planck equations for ion transport without assuming the existence of a diffusion boundary layer, numerically solved for the dispersion relation and performed extensive parameter sweeps over key parameters of interest such as surface energy and exchange current density.[149] Extending these two papers in 1998, Elezgaray, Léger and Argoul used a time-dependent base state under galvanostatic conditions, numerically solved for both the time-dependent base state and perturbed state to obtain the dispersion relation and demonstrated good agreement between their theory and experiments on copper electrodeposition in a thin gap cell.[150] The role of electrolyte additives in stabilizing electrodeposition was examined in the linear stability analysis performed by Haataja, Srolovitz and Bocarsly in 2002 and 2003,[151–153] and McFadden et al. in 2003.[154] By demonstrating that the effects of the anode can be ignored under certain conditions when deriving the dispersion relation, BuAli, Johns and Narayanan in 2006 simplified Sundström and Bark's analysis to obtain an analytical expression for the dispersion relation.[155] In 2004 and 2005, Monroe and Newman included additional mechanical effects such as pressure, viscous stress and deformational stress to the linear stability analysis of electrodeposition, which provided more stabilization beyond that provided by surface energy.[156,157] For a steady-state base state, in 2014, Tikekar, Archer and Koch studied how tethered immobilized anions provide additional stabilization to electrodeposition by reducing the electric field at the cathode and, after making some approximations, derived analytical expressions for the dispersion relation for small and large current densities.[158] Tikekar, Archer and Koch then extended this work in 2016 by accounting for elastic deformations that provide further stabilization.[159] Subsequently in 2018, Tikekar, Li, Archer and Koch looked at using polymer electrolyte viscosity to suppress morphological instabilities driven by electroconvection.[160] Building on Monroe and Newman's 2004 and 2005 work on interfacial deformation effects,[156,157] Ahmad and Viswanathan identified a new mechanism for stabilization driven by the difference of the metal density in the metal electrode and solid electrolyte in 2017,[161] and further generalized this work in the same year to account for anisotropy.[162] Natsiavas, Weinberg, Rosato and Ortiz in 2016 also investigated the stabilizing effect of prestress and showed good agreement between theory and experiment.[163] Relaxing the usual assumption of electroneutrality, in 2015, Nielsen and Bruus performed linear stability analysis for a steady-state base state that accounts for the extended space charge region that is formed when the electric double layer becomes nonequilibrium at an overlimiting current.[164]

Without performing a linear stability analysis, some models focus on describing the initiation and subsequent propagation of dendrites. The classic work in this class of models is by Chazalviel in 1990 in which they used the Poisson's equation for electrostatics, i.e., electroneutrality is not assumed, and showed that the initiation of ramified electrodeposits is caused by the creation of a space charge layer upon anion depletion at the cathode, the induction time for initiation is the time needed for building up this space charge layer, and the velocity of the ramified growth is equal to the electromigration velocity of the anions;[165] some experimental results were also obtained by Fleury, Chazalviel, Rosso and Sapoval in support of this model,[166] and some of the numerical results of the original analysis were subsequently improved by Rosso, Chazalviel and Chassaing.[167] Via an asymptotic analysis of the Poisson-Nernst-Planck equations for ion transport, Bazant also showed that the velocity of the ramified growth is approximately equal to the anion electromigration velocity and estimated the induction time for the onset of ramified growth.[168] Building on past theoretical and experimental work done on silver electrodeposition by Barton and Bockris,[169] and zinc electrodeposition by Despic, Diggle and Bockris,[170,171] Monroe and Newman investigated the propagation velocity and length of a dendrite tip that grows via Butler-Volmer kinetics.[172] By examining the thermodynamics and kinetics of heterogeneous nucleation and growth, which is assumed to proceed via the linearized Butler-Volmer equation valid for small overpotentials, Ely and García identified five different regimes of nucleus behavior.[173] Assuming a concentration-dependent electrolyte diffusivity and the existence of a hemispherical dendrite "precursor" that grows with Tafel kinetics, Akolkar studied the subsequent propagation velocity and length of the dendrite[174] and how they are affected by temperature.[175]

Contributions of this work.—In this paper, we perform linear stability analysis of electrodeposition inside a charged random porous medium, whose pore surface charges can generally be of any sign, that is filled with a liquid electrolyte and flanked on its sides by a pair of planar metal electrodes. The linear stability analysis is carried out with respect to a time-dependent base state and focuses on overlimiting current carried by surface conduction. By doing so, we combine and generalize previous work done in Refs. 149,150,158. For simplicity, we ignore bulk convection, electroosmotic flow, surface adsorption, surface diffusion of adsorbed species[139–142] and additional mechanical effects such as pressure, viscous stress and deformational stress.[156,157,159,161–163] We expect surface diffusion of adsorbed species, which alleviates electrodiffusion limitations, and interfacial deformation effects to stabilize electrodeposition, hence our work here can be considered a worst-case analysis. The only electrochemical reaction considered here is metal electrodeposition, therefore in the context of LMBs and LIBs, electrochemical and chemical reactions between lithium and the electrolyte that cause the formation of the solid electrolyte interphase (SEI) layer[176–179] are not included. We first derive governing equations for the full model that consists of coupling ion transport with electrochemical reaction kinetics, followed by applying linear stability analysis on the full model via the imposition of sinusoidal spatial perturbations around the time-dependent base state. For the dispersion relation, we perform a boundary layer analysis on the perturbed state to derive an accurate approximation for it and a convergence analysis of its full numerical solution. To better understand the physics of the dispersion relation, we carry out parameter sweeps over the pore surface charge density, Damköhler number and applied current density under galvanostatic conditions. We also compare the numerical and approximate solutions of the maximum wavenumber, maximum growth rate and critical wavenumber in order to verify the accuracy of these approximations. Subsequently, we apply the linear stability analysis to compare theoretical predictions and experimental data for copper electrodeposition in cellulose nitrate membranes,[180] and also use the stability analysis as a tool for investigating the dependence of crystal grain size on duty cycle during pulse electroplating.

Full Model

Transport.—The starting point for modeling ion transport is the leaky membrane model that is able to predict overlimiting current carried by surface conduction, which we have previously coupled with Butler-Volmer reaction kinetics for analyzing steady state current-voltage relations and linear sweep voltammetry.[181] The system under consideration is a binary asymmetric liquid electrolyte in a finite 3D charged random nanoporous medium where $x \in [0, L_x]$, $y \in \left[0, L_y\right]$ and $z \in [0, L_z]$, whose 2D projection is illustrated in Figure 1. We assume that the nanoporous medium is random with well connected pores such as cellulose nitrate membranes so that we can investigate macroscopic electrode-scale morphological instabilities.[180] The cations are electroactive and the anions are inert. Initially, at $t = 0$, the anode surface is located at $x = 0$ while the cathode surface is located at $x = L_x$. As is typical for linear stability analysis of electrodeposition,[149,150,164] we pick a moving reference frame with a velocity $u(t) = u_x(t)e_x$ that is equal to the velocity of the electrode/electrolyte interface so that the average positions of the dissolving anode and growing cathode remain stationary. For the porous medium, we denote its porosity, tortuosity, internal pore surface area per unit volume and pore surface charge per unit area as ϵ_p, τ, a_p and σ_s respectively. We assume that there are no homogeneous reactions and all material properties such as ϵ_p, τ, a_p and σ_s are constant and uniform. We also assume that dilute solution theory holds true, hence all activity coefficients are 1 and the cation and anion macroscopic diffusivities $D_{\pm0}$, where the 0 subscript indicates dilute limit, are constant, uniform and independent of concentrations. Accounting for corrections due to the tortuosity of the porous medium, the macroscopic diffusivity $D_{\pm0}$ is related to the molecular (free solution) diffusivity $D^m_{\pm0}$ by $D_{\pm0} = \frac{D^m_{\pm0}}{\tau}$.[182] The assumption of dilute solution theory further implies that the convective flux in the moving reference frame is negligible and the effect of the moving reference frame velocity $u(t) = u_x(t)e_x$ is only significant in the equation describing electrode surface growth or dissolution,[149,150,164] which we will discuss in Boundary conditions, constraints and initial conditions section. Under these assumptions, for ion transport, the Nernst-Planck equations describing species conservation, charge conservation equation and macroscopic electroneutrality constraint are given by

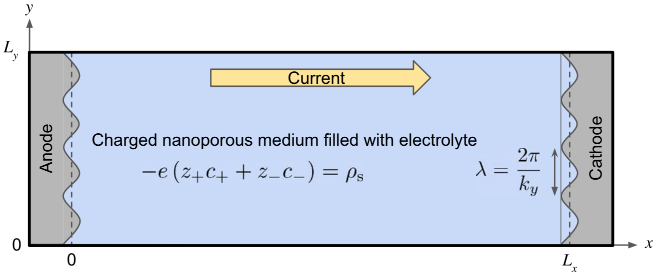

Figure 1. 2D projection of 3D system considered: charged random nanoporous medium filled with binary asymmetric liquid electrolyte where anode is on the left at $x = 0$ and cathode is on the right at $x = L_x$ along the x axis, which is the direction of the inter-electrode spacing, and y axis is the direction of the sinusoidal perturbation. $\lambda = \frac{2\pi}{k_y}$ is the perturbation wavelength where k_y is the wavenumber in the y direction. The linear stability analysis is actually performed in 3D in which the sinusoidal perturbation is applied in the y and z directions, and the extension of this 2D projection to the 3D case is straightforward. The current in the electrolyte flows from left to right. The equation shown on the left describes macroscopic electroneutrality given by Equation 3 where ρ_s is the volume-averaged background charge density.

$$\epsilon_p \frac{\partial c_\pm}{\partial t} + \nabla \cdot F_\pm = 0, \quad F_\pm = -\epsilon_p D_{\pm0}\left(\nabla c_\pm + \frac{z_\pm e c_\pm}{k_B T}\nabla\phi\right), \tag{1}$$

$$\nabla \cdot J = 0, \quad J = e(z_+F_+ + z_-F_-), \tag{2}$$

$$\rho_s = \frac{\sigma_s}{h_p} = \frac{a_p\sigma_s}{\epsilon_p} = -e(z_+c_+ + z_-c_-), \tag{3}$$

where $c_\pm$, $F_\pm$, $z_\pm$, are the cation and anion concentrations, fluxes and charge numbers respectively, ϕ is the electrolyte electric potential, J is the electrolyte current density, $h_p = \frac{\epsilon_p}{a_p}$ is the effective pore size and ρ_s is the volume-averaged background charge density. Denoting the numbers of cations and anions that are formed from complete dissociation of 1 molecule of neutral salt as $\nu_\pm$, electroneutrality requires that $z_+\nu_+ + z_-\nu_- = 0$. We will use the macroscopic electroneutrality constraint given by Equation 3 to eliminate c_+ as a dependent variable, therefore leaving c_- and ϕ as the remaining dependent variables.

For a classical system with an uncharged nanoporous medium, i.e., $\rho_s = 0$, the maximum current density that the system can possibly attain under electrodiffusion is called the diffusion-limited or limiting current density J_{lim}, which is given by[181]

$$J_{\text{lim}} = \frac{2(z_+ - z_-)e\epsilon_p D_{+0}\nu_- c_0}{L_x} \tag{4}$$

where c_0 is the neutral salt bulk concentration. The limiting current I_{lim} is then given by $I_{\text{lim}} = J_{\text{lim}}A$ where $A = L_yL_z$ is the surface area of the electrode. Under galvanostatic conditions, when a current density J_a larger than J_{lim} is applied, the cation and anion concentrations at the cathode reach 0 and the electrolyte electric potential and electric field there diverge in finite time, which is called Sand's time[183] denoted as t_s; see[184] for a discussion of some subtlety associated with this transition time when J_a is exactly equal to J_{lim}. If we have not assumed macroscopic electroneutrality and instead modeled electric double layers that can go out of equilibrium at high currents and voltages, then the electric field would be large but finite at and past t_s.[8,164,185,186] Defining the dimensionless Sand's time $\tilde{t}_s = \frac{D_{\text{amb0}}t_s}{L_x^2}$ and dimensionless applied current density $\tilde{J}_{\mathrm{a}} = \frac{J_{\mathrm{a}}}{J_{\mathrm{lim}}}$ where $D_{\mathrm{amb0}} = \frac{(z_{+}-z_{-})D_{+0}D_{-0}}{z_{+}D_{+0}-z_{-}D_{-0}}$[103,181] is the ambipolar diffusivity of the neutral salt in the dilute limit and $\frac{L_x^2}{D_{\mathrm{amb0}}}$ is the diffusion time scale, $\tilde{t}_{\mathrm{s}}$ is given by[184]

$$\tilde{t}_{\mathrm{s}} = \frac{\pi}{16\tilde{J}_{\mathrm{a}}^2}, \quad \tilde{J}_{\mathrm{a}} > 1. \qquad [5]$$

For galvanostatic conditions, t_{s} is a critically important time scale because the formation of dendrites often occurs near or at t_{s}, therefore it will be central to the linear stability analysis results discussed in Results section.

Unlike the classical case of $\rho_{\mathrm{s}} = 0$, for $\rho_{\mathrm{s}} < 0$, the system can sustain an overlimiting current $\tilde{J}_{\mathrm{a}} > 1$ via surface conduction that is the electromigration of the counterions in the electric double layers (EDLs), which are formed next to the charged pore surfaces, under a large electric field generated in the depletion region next to the cathode. This additional surface conductivity thus enables the system to go beyond t_{s} and eventually reach a steady state, in stark contrast to the finite time divergence of the classical case at t_{s}. On the other hand, for $\rho_{\mathrm{s}} > 0$, the counterions in the EDLs are the inert anions instead of the electroactive cations, which contribute a surface current that flows in the opposite direction from that of the bulk current. Because of this "negative" surface conductivity conferred by $\rho_{\mathrm{s}} > 0$ relative to $\rho_{\mathrm{s}} = 0$, at the cathode, the bulk electrolyte concentration vanishes and the electric field diverges earlier than t_{s}; in other words, $\rho_{\mathrm{s}} > 0$ effectively reduces t_{s}. A more quantitative way of explaining this is that the "negative" surface conductivity causes the maximum current density that can be achieved, which is denoted as J_{max}, to be smaller than J_{lim}, and J_{max} decreases as ρ_{s} increases. In effect, a more positive ρ_{s} decreases J_{lim}, which thus leads to a smaller t_{s} for a given J_{a} according to Equation 5. Details of how to numerically compute J_{max} are found in Ref. 181; note that J_{max} here corresponds to $I_{\mathrm{max}}^{\mathrm{BV}}$ in Ref. 181.

Electrochemical reaction kinetics.—In order to analyze how spatial perturbations of an electrode surface affect its linear stability, we need to account for the effects of surface curvature and surface energy in the electrochemical reaction kinetics model. The mean curvature of the electrode/electrolyte interface $\mathscr{H}$ is given by $\mathscr{H} = -\frac{1}{2}\nabla_{\mathrm{s}} \cdot \hat{n}$ where ∇_{s} is the surface gradient operator and $\hat{n}$ is the unit normal that points outwards from the electrolyte.[187] In this paper, we consider a charge transfer reaction that involves only the cations and electrons while the anions are inert. More concretely, we suppose the following charge transfer reaction consuming n electrons $\mathrm{O}^{z_{\mathrm{O}}} + n\mathrm{e}^{-} \rightleftharpoons \mathrm{R}^{z_{\mathrm{R}}}$ where $\mathrm{O}^{z_{\mathrm{O}}}$ is the oxidized species O with charge z_{O}, e^{-} is the electron e with charge -1, $\mathrm{R}^{z_{\mathrm{R}}}$ is the reduced species R with charge z_{R}, and $z_{\mathrm{O}} - n = z_{\mathrm{R}}$ because of charge conservation. If the reduced species is solid metal, i.e., $z_{\mathrm{R}} = 0$, as is the case in metal electrodeposition, the creation of additional electrode/electrolyte interfacial area results in a surface energy penalty that appears in the electrochemical potential of the reduced species. Therefore, the electrochemical potentials μ_i of the oxidized species O, electron e and reduced species R for $i \in \{\mathrm{O}, \mathrm{e}, \mathrm{R}\}$ are given by

$$\mu_{\mathrm{O}} = k_{\mathrm{B}}T \ln a_{\mathrm{O}} + z_{\mathrm{O}}e\phi + \mu_{\mathrm{O}}^{\ominus}, \qquad [6]$$

$$\mu_{\mathrm{e}} = k_{\mathrm{B}}T \ln a_{\mathrm{e}} - e\phi_{\mathrm{e}} + \mu_{\mathrm{e}}^{\ominus}, \qquad [7]$$

$$\mu_{\mathrm{R}} = k_{\mathrm{B}}T \ln a_{\mathrm{R}} + z_{\mathrm{R}}e\phi + \mu_{\mathrm{R}}^{\ominus} + 2\Omega\gamma\mathscr{H}, \qquad [8]$$

where the surface energy term $2\Omega\gamma\mathscr{H}$[149,150,156–158,164,172,187] is included in μ_{R} when the reduced species is solid metal ($z_{\mathrm{R}} = 0$) and the $\ominus$ superscript indicates standard state. The activity of species i is given by $a_i = \gamma_i\hat{c}_i$ where γ_i is the activity coefficient of species i and $\hat{c}_i = \frac{c_i}{c_i^{\ominus}}$ is the concentration of species i normalized by its standard concentration $c_i^{\ominus}$. $\mu_i^{\ominus}$ is the standard electrochemical potential of species i, ϕ_{e} is the electrode electric potential, $\Omega = \frac{M_{\mathrm{m}}}{\rho_{\mathrm{m}}}$ is the atomic volume of the solid metal where M_{m} and ρ_{m} are the atomic mass and mass density of the metal respectively, and γ is the isotropic surface energy of the metal/electrolyte interface. The quantity $\frac{\Omega\gamma}{k_{\mathrm{B}}T}$ is the capillary constant that has units of length.[22–24] The interfacial electric potential difference $\Delta\phi$ is defined as $\Delta\phi = \phi_{\mathrm{e}} - \phi$. At equilibrium when $\mu_{\mathrm{O}} + n\mu_{\mathrm{e}} = \mu_{\mathrm{R}}$, we obtain the Nernst equation

$$\Delta\phi^{\mathrm{eq}} = \frac{k_{\mathrm{B}}T}{ne} \ln \frac{a_{\mathrm{O}}a_{\mathrm{e}}^{n}}{a_{\mathrm{R}}} + E^{\ominus} - \frac{2\Omega\gamma\mathscr{H}}{ne}, \quad E^{\ominus} = \frac{\mu_{\mathrm{O}}^{\ominus} + n\mu_{\mathrm{e}}^{\ominus} - \mu_{\mathrm{R}}^{\ominus}}{ne}, \qquad [9]$$

where the "eq" superscript denotes equilibrium and $E^{\ominus}$ is the standard electrode potential. When the system is driven out of equilibrium so that $\mu_{\mathrm{O}} + n\mu_{\mathrm{e}} \neq \mu_{\mathrm{R}}$, the system generates a faradaic current density J_{F} that is given by[25,26,182]

$$J_{\mathrm{F}} = nek_0\left[\exp\left(-\frac{\mu_{\ddagger}^{\mathrm{r,ex}} - \mu_{\mathrm{O}} - n\mu_{\mathrm{e}}}{k_{\mathrm{B}}T}\right) - \exp\left(-\frac{\mu_{\ddagger}^{\mathrm{r,ex}} - \mu_{\mathrm{R}}}{k_{\mathrm{B}}T}\right)\right] \qquad [10]$$

where k_0 is the overall reaction rate constant and $\mu_{\ddagger}^{\mathrm{r,ex}}$ is the excess electrochemical potential of the transition state for the faradaic reaction. Using the Butler-Volmer hypothesis, $\mu_{\ddagger}^{\mathrm{r,ex}}$ consists of a chemical contribution $k_{\mathrm{B}}T \ln \gamma_{\ddagger}^{\mathrm{r}}$, where $\gamma_{\ddagger}^{\mathrm{r}}$ is the activity coefficient of the transition state for the faradaic reaction, and a convex combination of the electrostatic energies, surface energies (only for the reduced species) and standard electrochemical potentials weighted by α, which is the charge transfer coefficient. Therefore, $\mu_{\ddagger}^{\mathrm{r,ex}}$ is given by

$$\begin{aligned}\mu_{\ddagger}^{\mathrm{r,ex}} &= k_{\mathrm{B}}T \ln \gamma_{\ddagger}^{\mathrm{r}} + (1-\alpha)\left(z_{\mathrm{O}}e\phi - ne\phi_{\mathrm{e}} + \mu_{\mathrm{O}}^{\ominus} + n\mu_{\mathrm{e}}^{\ominus}\right) \\ &\quad + \alpha\left(z_{\mathrm{R}}e\phi + \mu_{\mathrm{R}}^{\ominus} + 2\Omega\gamma\mathscr{H}\right). \end{aligned} \qquad [11]$$

Defining the overpotential η as $\eta = \frac{\mu_{\mathrm{R}} - \mu_{\mathrm{O}} - n\mu_{\mathrm{e}}}{ne} = \Delta\phi - \Delta\phi^{\mathrm{eq}}$, we rewrite J_{F} as

$$\begin{aligned} J_{\mathrm{F}} &= j_0\left\{\exp\left(-\frac{\alpha ne\eta}{k_{\mathrm{B}}T}\right) - \exp\left[\frac{(1-\alpha)ne\eta}{k_{\mathrm{B}}T}\right]\right\}, \\ j_0 &= \frac{k_0 ne\left(a_{\mathrm{O}}a_{\mathrm{e}}^{n}\right)^{1-\alpha}a_{\mathrm{R}}^{\alpha}}{\gamma_{\ddagger}^{\mathrm{r}}}, \end{aligned} \qquad [12]$$

where j_0 is the exchange current density. In this form, we can identify the cathodic and anodic charge transfer coefficients, which are denoted as α_{c} and α_{a} respectively, as $\alpha_{\mathrm{c}} = \alpha$ and $\alpha_{\mathrm{a}} = 1 - \alpha$ such that $\alpha_{\mathrm{c}} + \alpha_{\mathrm{a}} = 1$. We note that our particular choice of $\mu_{\ddagger}^{\mathrm{r,ex}}$ in Equation 11 corresponds to choosing the "mechanical transfer coefficient" α_{m} defined in Ref. 156 to be equal to α_{a}, causing j_0 to not depend explicitly on $\mathscr{H}$.

In this paper, we assume that the only charge transfer reaction occurring is metal electrodeposition that happens via the electrochemical reduction of cations in the electrolyte to solid metal on the electrode. The activity of solid metal is 1 while we assume that the activity of electrons is 1. In addition, like in Transport section, we assume that dilute solution theory is applicable, therefore the activity coefficients of the cation, anion and transition state for the faradaic reaction are 1 and we replace activities of the cation and anion with their normalized concentrations $\hat{c}_{\pm}$. Therefore, $\Delta\phi^{\mathrm{eq}}$ and j_0 simplify to

$$\Delta\phi^{\mathrm{eq}} = \frac{k_{\mathrm{B}}T}{ne} \ln \hat{c}_{+} + E^{\ominus} - \frac{2\Omega\gamma\mathscr{H}}{ne}, \quad j_0 = k_0 ne\hat{c}_{+}^{1-\alpha}. \qquad [13]$$

To compare the reaction and diffusion rates, we define the Damköhler number Da as the ratio of the faradaic current density scale $e\epsilon_{\mathrm{p}}k_0$ and limiting current density J_{lim} given by

$$\mathrm{Da} = \frac{e\epsilon_{\mathrm{p}}k_0}{J_{\mathrm{lim}}}. \qquad [14]$$

When Da is large, i.e., $\mathrm{Da} \gg 1$, the system is diffusion-limited but when Da is small, i.e., $\mathrm{Da} \ll 1$, the system is reaction-limited.

Boundary conditions, constraints and initial conditions.—We use "a" and "c" superscripts to denote the anode and cathode respectively, $r = [x, y, z]^{\mathrm{T}}$ to denote the position vector, and $r_{\mathrm{m}}^{\mathrm{a,c}} = \left[x_{\mathrm{m}}^{\mathrm{a,c}}, y_{\mathrm{m}}^{\mathrm{a,c}}, z_{\mathrm{m}}^{\mathrm{a,c}}\right]^{\mathrm{T}}$ to denote the positions of the anode and cathode. We ground the anode at all times, i.e., $\phi_{\mathrm{e}}^{\mathrm{a}} = 0$. Because the cations are electroactive, we impose no-flux boundary conditions for the cation flux on all boundaries except the anode and cathode where faradaic reactions involving the cations occur. On the other hand, because the anions are inert, we impose no-flux boundary conditions for the anion flux on all boundaries. At the anode and cathode, we require the conservation of charges across the electrode/electrolyte interfaces. In summary, the boundary conditions are given by $\hat{n} \cdot F_{-}\left(r = r_{\mathrm{m}}^{\mathrm{a,c}}\right) = 0$, $\hat{n} \cdot J\left(r = r_{\mathrm{m}}^{\mathrm{a,c}}\right) = \epsilon_{\mathrm{p}} J_{\mathrm{F}}^{\mathrm{a,c}}$, $\hat{n} \cdot F_{-}(r = r_{\mathrm{other}}) = 0$ and $\hat{n} \cdot J(r = r_{\mathrm{other}}) = 0$ where r_{other} refers to all boundaries except the anode and cathode.

The velocity of the electrode/electrolyte interface $v_{\mathrm{I}}^{\mathrm{a,c}}$ is defined as $v_{\mathrm{I}}^{\mathrm{a,c}} = \epsilon_{\mathrm{p}} \frac{\mathrm{d}r_{\mathrm{m}}^{\mathrm{a,c}}}{\mathrm{d}t}$ and its normal component $v_{\mathrm{In}}^{\mathrm{a,c}}$ is given by $v_{\mathrm{In}}^{\mathrm{a,c}} = \hat{n} \cdot v_{\mathrm{I}}^{\mathrm{a,c}} = \epsilon_{\mathrm{p}} \hat{n} \cdot \frac{\mathrm{d}r_{\mathrm{m}}^{\mathrm{a,c}}}{\mathrm{d}t}$. Because the growth (dissolution) of the electrode surface is caused by metal electrodeposition (electrodissolution), taking into account the moving reference frame velocity $u(t) = u_x(t) e_x$, the normal interfacial velocity is related to the normal current density by $v_{\mathrm{In}}^{\mathrm{a,c}} = -\frac{\Omega \hat{n} \cdot J\left(r = r_{\mathrm{m}}^{\mathrm{a,c}}\right)}{z_{+} e} - \hat{n} \cdot u\left(r = r_{\mathrm{m}}^{\mathrm{a,c}}\right)$ and therefore, $\epsilon_{\mathrm{p}} \hat{n} \cdot \frac{\mathrm{d}r_{\mathrm{m}}^{\mathrm{a,c}}}{\mathrm{d}t} = -\frac{\Omega \hat{n} \cdot J\left(r = r_{\mathrm{m}}^{\mathrm{a,c}}\right)}{z_{+} e} - \hat{n} \cdot u\left(r = r_{\mathrm{m}}^{\mathrm{a,c}}\right)$.

For galvanostatic conditions in which we apply a current I_{a} on the system, we require $\int \hat{n} \cdot J\left(r = r_{\mathrm{m}}^{\mathrm{c}}\right) \mathrm{d}S^{\mathrm{c}} = \int -\hat{n} \cdot J\left(r = r_{\mathrm{m}}^{\mathrm{a}}\right) \mathrm{d}S^{\mathrm{a}} = I_{\mathrm{a}}$ to satisfy charge conservation whereas for potentiostatic conditions in which we apply an electric potential V on the cathode, we set $\phi_{\mathrm{e}}^{\mathrm{c}} = V$. For initial conditions, we set $c_{-}(t = 0) = \nu_{-} c_0 - \frac{\rho_{\mathrm{s}} + |\rho_{\mathrm{s}}|}{2 z_{-} e} \equiv \beta_1$ where c_0 is the initial neutral salt bulk concentration,[181] and $x_{\mathrm{m}}^{\mathrm{a}}(t = 0) = 0$ and $x_{\mathrm{m}}^{\mathrm{c}}(t = 0) = L_x$, i.e., the anode and cathode are initially planar.

Linear Stability Analysis

Perturbations and linearization.—Linear stability analysis generally involves imposing a spatial perturbation around a base state, keeping constant and linear terms of the perturbed state, and determining the dispersion relation that relates the growth rate of the perturbation to its wavenumber or wavelength. For electrodeposition specifically, the objective is to impose a spatial perturbation on a planar electrode surface and determine the effects of key system parameters on the linear stability of the surface in response to this perturbation. In this paper, we will choose a time-dependent base state, therefore the dispersion relation is also time-dependent. In 3D, the electrode/electrolyte interface can be written explicitly as $x = h(y, z, t)$ where h is the electrode surface height. Given h, we can derive explicit expressions for surface variables such as the curvature $\mathscr{H}$ and normal interfacial velocity v_{In} in terms of h and its spatial and temporal derivatives,[187,188] which are provided in Section I of Supplementary Material. For brevity, we let $k = \left[k_y, k_z\right]^{\mathrm{T}}$ and $\xi = [y, z]^{\mathrm{T}}$ where k is the wavevector, and k_y and k_z are the wavenumbers in the y and z directions respectively. Therefore, $k \cdot \xi = k_y y + k_z z$, $k^2 = \|k\|_2^2 = k_y^2 + k_z^2$ where $\|\cdot\|_2$ is the L^2-norm and $\|k\|_2$ is the overall wavenumber, and the wavelength λ is given by $\lambda = \frac{2\pi}{\|k\|_2}$. For brevity again, we write the overall wavenumber as k and it is obvious from context whether k refers to the wavevector or overall wavenumber. The perturbation that will be imposed is sinusoidal in the y and z directions given by

$$h(\xi, t) = h^{(0)}(t) + \epsilon \Re\left[h^{(1)} \exp(ik \cdot \xi + \omega t)\right] + \mathcal{O}\left(\epsilon^2\right) \tag{15}$$

where $\epsilon \ll 1$ is a dimensionless small parameter, the (0) and (1) superscripts denote the base and perturbed states respectively, $\Re(\cdot)$ gives the real part of a complex number, $h^{(1)}$ is the complex-valued perturbation amplitude of the electrode surface height, and ω is the complex-valued growth rate of the perturbation. In response to such an electrode surface perturbation, we assume that the perturbations to c_{-} and ϕ are similarly given by

$$c_{-}(x, \xi, t) = c_{-}^{(0)}(x, t) + \epsilon \Re\left[c_{-}^{(1)}(x) \exp(ik \cdot \xi + \omega t)\right] + \mathcal{O}\left(\epsilon^2\right), \tag{16}$$

$$\phi(x, \xi, t) = \phi^{(0)}(x, t) + \epsilon \Re\left[\phi^{(1)}(x) \exp(ik \cdot \xi + \omega t)\right] + \mathcal{O}\left(\epsilon^2\right), \tag{17}$$

where $c_{-}^{(1)}$ and $\phi^{(1)}$ are the complex-valued perturbation amplitudes of anion concentration and electrolyte electric potential respectively.

To evaluate c_{-} and ϕ and their gradients ∇c_{-} and $\nabla \phi$ at the interface at $x = h$, we require their Taylor series expansions around the base state interface at $x = h^{(0)}$. Letting $\hat{\epsilon} = \epsilon \exp(ik \cdot \xi + \omega t)$ and $\theta \in \{c_{-}, \phi\}$, these expansions are given by[149,150,164]

$$\theta(x = h) = \theta^{(0)}\left(x = h^{(0)}\right) + \hat{\epsilon}\left(h^{(1)} \frac{\partial \theta^{(0)}}{\partial x} + \theta^{(1)}\right)\Bigg|_{x = h^{(0)}} + \mathcal{O}\left(\epsilon^2\right), \tag{18}$$

$$\frac{\partial \theta}{\partial x}(x = h) = \frac{\partial \theta^{(0)}}{\partial x}\left(x = h^{(0)}\right) + \hat{\epsilon}\left(h^{(1)} \frac{\partial^2 \theta^{(0)}}{\partial x^2} + \frac{\mathrm{d}\theta^{(1)}}{\mathrm{d}x}\right)\Bigg|_{x = h^{(0)}} + \mathcal{O}\left(\epsilon^2\right), \tag{19}$$

$$\begin{aligned} \frac{\partial \theta}{\partial y}(x = h) &= \hat{\epsilon} i k_y \theta^{(1)}\left(x = h^{(0)}\right) + \mathcal{O}\left(\epsilon^2\right), \\ \frac{\partial \theta}{\partial z}(x = h) &= \hat{\epsilon} i k_z \theta^{(1)}\left(x = h^{(0)}\right) + \mathcal{O}\left(\epsilon^2\right), \end{aligned} \tag{20}$$

$$\nabla \theta(x = h) = \frac{\partial \theta}{\partial x}(x = h) e_x + \frac{\partial \theta}{\partial y}(x = h) e_y + \frac{\partial \theta}{\partial z}(x = h) e_z + \mathcal{O}\left(\epsilon^2\right). \tag{21}$$

After substituting these perturbation expressions into the full model in Full model section, we obtain the base and perturbed states by matching the $\mathcal{O}(1)$ and $\mathcal{O}(\epsilon)$ terms respectively. The dispersion relation $\omega(k)$ is subsequently computed by solving these $\mathcal{O}(1)$ and $\mathcal{O}(\epsilon)$ equations. The growth rate ω is generally complex-valued and for a particular k value, there is an infinite discrete spectrum of ω values. However, for linear stability analysis, we are primarily interested in the maximum of the real parts of the ω values, which is denoted as $\max\{\Re(\omega)\}$, that corresponds to the most unstable eigenmode. If $\max\{\Re(\omega)\} < 0$, the perturbation decays exponentially in time and the base state is linearly stable. On the other hand, if $\max\{\Re(\omega)\} > 0$, the perturbation grows exponentially in time and the base state is linearly unstable. Lastly, if $\max\{\Re(\omega)\} = 0$, the perturbation does not decay nor grow and the base state is marginally stable. The imposition of the boundary conditions at $r = r_{\mathrm{other}}$ described in Boundary conditions, constraints and initial conditions section results in the quantization of the set of valid wavenumbers, which is explained in detail in Section IIIC of Supplementary Material.

Nondimensionalization.—To make the equations more compact and derive key dimensionless parameters, in Table I, we define the scales that are used for nondimensionalizing the full model in Full model section and the perturbation expressions in Perturbations and linearization section. $\tilde{L}_y$ and $\tilde{L}_z$ are the aspect ratios in the y and z directions respectively. For convenience, we also define $\beta_{\mathrm{D}} = -\frac{z_{-} D_{-0}}{2\left(z_{+} D_{+0} - z_{-} D_{-0}\right)}$ (weighted ratio of cation and anion diffusivities), $\beta_{\mathrm{m}} = \nu_{+} c_0 \Omega$ (ratio of atomic volume of solid metal to reciprocal electrolyte concentration), $\beta_{\mathrm{v}} = \frac{\beta_{\mathrm{m}}}{\beta_{\mathrm{D}}}$ and $\xi_{+} = \frac{\nu_{+} c_0}{c_{+}^{\Theta}}$ (ratio of electrolyte concentration to standard cation concentration), and note that $\hat{c}_{+} = \xi_{+}(\tilde{c}_{-} - \tilde{\rho}_{\mathrm{s}})$. Two important dimensionless parameters emerge from this nondimensionalization process, namely the Damköhler number $\mathrm{Da} = \tilde{k}_0$ that is described earlier in Equation 14 and the capillary number Ca that is given by

$$\mathrm{Ca} = \tilde{\gamma} = \frac{\Omega \gamma}{L_x k_{\mathrm{B}} T}, \tag{22}$$

which is the ratio of the capillary constant $\frac{\Omega \gamma}{k_{\mathrm{B}} T}$[22–24] to the interelectrode distance L_x, and $\tilde{\gamma}$ is the dimensionless isotropic surface energy of the metal/electrolyte interface.

To avoid cluttering the notation, we drop tildes for all dimensionless variables and parameters, and all variables and parameters are

Table I. Scales used for nondimensionalization.

Variables and parameters	Scale
$x, y, z, L_y, L_z, r, r_\mathrm{m}, h, \lambda, \xi$	L_x
t	$\frac{L_x^2}{D_\mathrm{amb0}}$ (diffusion time)
$c_\pm$	$\nu_\pm c_0$
$\phi, \phi_\mathrm{e}, \Delta\phi^\mathrm{eq}, E^\Theta, \Delta\phi, \eta$	$\frac{k_\mathrm{B}T}{e}$ (thermal voltage)
$D_{\pm 0}$	D_amb0
ρ_s	$z_+\nu_+ec_0 = -z_-\nu_-ec_0$
$F_\pm$	$\frac{\epsilon_\mathrm{p}D_\mathrm{amb0}\nu_\pm c_0}{L_x}$
$u, u_x, v_\mathrm{I}, v_\mathrm{In}$	$\frac{\epsilon_\mathrm{p}D_\mathrm{amb0}}{L_x}$
J	J_lim
I	I_lim
j_0, J_F	$\frac{J_\mathrm{lim}}{\epsilon_\mathrm{p}}$
k_0	$\frac{J_\mathrm{lim}}{e\epsilon_p}$
γ	$\frac{L_xk_\mathrm{B}T}{\Omega}$
$\mathscr{H}, k_y, k_z, k$	$\frac{1}{L_x}$
ω	$\frac{D_\mathrm{amb0}}{L_x^2}$ (reciprocal diffusion time)

dimensionless in the following sections unless otherwise stated. We also rewrite the (0) and (1) superscripts, which denote the base and perturbed states respectively, as 0 and 1 subscripts respectively. Similarly, we drop the 0 subscript for diffusivities and the − subscript for anion-related variables and parameters. As shorthand, we use subscripts to denote partial derivatives with respect to x (with the exception that u_x denotes the x component of the moving reference frame velocity u), y, z and t, primes to denote total derivatives with respect to x, and an overhead dot to denote the total derivative with respect to t. All equations for the dimensionless full model are provided in Section II of Supplementary Material. Details for deriving the dimensionless equations for the base and perturbed states are provided in Section III of Supplementary Material, and we summarize them in Base state and Perturbed state sections below.

Base state.—The equations for the base state are obtained by substituting the perturbation expressions in Perturbations and linearization section into the full model in Full model section and matching terms at $\mathcal{O}(1)$. Equivalently, the base state is simply the full model specialized to 1D in the x direction with the curvature-related terms dropped, which only appear at $\mathcal{O}(\epsilon)$. Therefore, at $\mathcal{O}(1)$, the governing PDEs (partial differential equations) are given by

$$c_{0,t} - D\left[c_{0,xx} + z\left(c_0\phi_{0,x}\right)_x\right] = 0, \qquad [23]$$

$$\beta_\mathrm{D}\left[(D-D_+)c_{0,xx} + z_+D_+\rho_\mathrm{s}\phi_{0,xx} - (z_+D_+ - zD)\left(c_0\phi_{0,x}\right)_x\right] = 0, \qquad [24]$$

where the first PDE is the Nernst-Planck equation describing species conservation of anions and the second PDE is the charge conservation equation. The boundary conditions at the anode at $x = h_0^\mathrm{a}$ are given by

$$\phi_\mathrm{e}^\mathrm{a} = 0, \qquad [25]$$

$$-D\left(-c_{0,x} - zc_0\phi_{0,x}\right) = 0, \qquad [26]$$

$$\hat{n}\cdot J_0 = j_{0,0}\{\exp(-\alpha n\eta_0) - \exp[(1-\alpha)n\eta_0]\}, \qquad [27]$$

$$-\dot{h}_0 = -\beta_\mathrm{v}\hat{n}\cdot J_0 + u_x, \qquad [28]$$

where $\eta_0 = \phi_\mathrm{e} - \phi_0 - \frac{1}{n}\ln\left[\xi_+(c_0-\rho_\mathrm{s})\right] - E^\Theta$, $j_{0,0} = \mathrm{Da}n[\xi_+(c_0-\rho_\mathrm{s})]^{1-\alpha}$ and $\hat{n}\cdot J_0 = \beta_\mathrm{D}[-(D-D_+)c_{0,x} - z_+D_+\rho_\mathrm{s}\phi_{0,x} + (z_+D_+ - zD)c_0\phi_{0,x}]$. Since the unit normal at the cathode points in the opposite direction from that at the anode, the signs of the expressions involving $\hat{n}$ at the cathode are opposite to that at the anode. Therefore, the boundary conditions at the cathode at $x = h_0^\mathrm{c}$ are given by

$$-D\left(c_{0,x} + zc_0\phi_{0,x}\right) = 0, \qquad [29]$$

$$\hat{n}\cdot J_0 = j_{0,0}\{\exp(-\alpha n\eta_0) - \exp[(1-\alpha)n\eta_0]\}, \qquad [30]$$

$$\dot{h}_0 = -\beta_\mathrm{v}\hat{n}\cdot J_0 - u_x, \qquad [31]$$

where $\eta_0 = \phi_\mathrm{e} - \phi_0 - \frac{1}{n}\ln[\xi_+(c_0-\rho_\mathrm{s})] - E^\Theta$, $j_{0,0} = \mathrm{Da}n[\xi_+(c_0-\rho_\mathrm{s})]^{1-\alpha}$ and $\hat{n}\cdot J_0 = \beta_\mathrm{D}[(D-D_+)c_{0,x} + z_+D_+\rho_\mathrm{s}\phi_{0,x} - (z_+D_+ - zD)c_0\phi_{0,x}]$.

We pick $u_x\left(x = h_0^\mathrm{a}\right)$ and $u_x\left(x = h_0^\mathrm{c}\right)$ such that the positions of the anode and cathode in the base state remain stationary, i.e., $\dot{h}_0^\mathrm{a} = \dot{h}_0^\mathrm{c} = 0$. Therefore, $u_x = \beta_\mathrm{v}\hat{n}\cdot J_0\left(x = h_0^\mathrm{a}\right) = -\beta_\mathrm{v}\hat{n}\cdot J_0\left(x = h_0^\mathrm{c}\right)$ where the second equality automatically holds true because of charge conservation in the 1D $\mathcal{O}(1)$ base state. Physically, u_x is equal to the velocity of the growing planar cathode/electrolyte interface or the dissolving planar anode/electrolyte interface in the base state. The initial conditions are given by

$$c_0(t=0) = \beta_1, \quad h_0^\mathrm{a}(t=0) = 0, \quad h_0^\mathrm{c}(t=0) = 1. \qquad [32]$$

Since $\dot{h}_0^\mathrm{a} = \dot{h}_0^\mathrm{c} = 0$, $h_0^\mathrm{a}(t) = 0$ and $h_0^\mathrm{c}(t) = 1$ at all t. For galvanostatic conditions in which we apply a current density J_a on the system, we impose

$$J_\mathrm{a} = \beta_\mathrm{D}\left[(D-D_+)c_{0,x} + z_+D_+\rho_\mathrm{s}\phi_{0,x} - (z_+D_+ - zD)c_0\phi_{0,x}\right]\Big|_{x=h_0^\mathrm{c}} \qquad [33]$$

$$= \beta_\mathrm{D}\left[(D-D_+)c_{0,x} + z_+D_+\rho_\mathrm{s}\phi_{0,x} - (z_+D_+ - zD)c_0\phi_{0,x}\right]\Big|_{x=h_0^\mathrm{a}}. \qquad [34]$$

For potentiostatic conditions in which we apply an electric potential V on the cathode, we impose $\phi_\mathrm{e}^\mathrm{c} = V$.

The equations for the time-dependent base state cannot generally be solved analytically, therefore we would have to solve them numerically. However, at steady state, the base state admits semi-analytical solutions for any ρ_s.[181] Specifically, c_0, $\phi_{0,x}$ and their spatial derivatives can be analytically expressed in terms of the Lambert W function.[189] On the other hand, ϕ_0 is known semi-analytically because it can be analytically expressed in terms of the Lambert W function up to an additive constant, which is a function of J_a and ρ_s and is found by numerically solving the algebraic Butler-Volmer equations given by Equations 27 and 30 with MATLAB's `fsolve` or `fzero` function.

Perturbed state.—To derive the equations for the perturbed state at $\mathcal{O}(\epsilon)$, we substitute the perturbation expressions in Perturbations and linearization section into the full model in Full model section and match terms at $\mathcal{O}(\epsilon)$. One important outcome is that the curvature-related terms appear as functions of k^2 because they are associated with second-order spatial partial derivatives in the y and z directions. At $\mathcal{O}(\epsilon)$, the governing ODEs (ordinary differential equations) are given by

$$D\left\{c_1'' - k^2c_1 + z\left[\left(c_0\phi_1' + \phi_{0,x}c_1\right)_x - k^2c_0\phi_1\right]\right\} = \omega c_1, \qquad [35]$$

$$\begin{aligned}(D-D_+)\left(c_1'' - k^2c_1\right) + z_+D_+\rho_\mathrm{s}\left(\phi_1'' - k^2\phi_1\right)& \\ - (z_+D_+ - zD)\left[\left(c_0\phi_1' + \phi_{0,x}c_1\right)_x - k^2c_0\phi_1\right] = 0,& \qquad [36]\end{aligned}$$

where the first ODE describes the perturbation in species conservation of anions and the second ODE describes the perturbation in charge conservation. For brevity, we define $\alpha_3 = -\alpha\exp(-\alpha n\eta_0) -$

$(1-\alpha)\exp[(1-\alpha)n\eta_0]$. The boundary conditions at the anode at $x = h_0^{\mathrm{a}}$ are given by

$$c_{0,t}h_1^{\mathrm{a}} - D\left[-c_1' - z\left(c_0\phi_1' + \phi_{0,x}c_1\right)\right] = 0, \qquad [37]$$

$$\beta_{\mathrm{v}} j_{0,0}\left(\hat{D}_1 h_1^{\mathrm{a}} + \hat{D}_2 c_1 + \hat{D}_3\phi_1\right) = \omega h_1^{\mathrm{a}}, \qquad [38]$$

$$\begin{aligned}\beta_{\mathrm{m}}[&-(D-D_+)c_1' - z_+D_+\rho_{\mathrm{s}}\phi_1' \\ &+ (z_+D_+ - zD)\left(c_0\phi_1' + \phi_{0,x}c_1\right)] = \omega h_1^{\mathrm{a}},\end{aligned} \qquad [39]$$

where the $\hat{D}_1$, $\hat{D}_2$ and $\hat{D}_3$ parameters are

$$\hat{D}_1 = \alpha_3 n\left(-\phi_{0,x} + \frac{\gamma k^2}{n}\right) + \frac{\exp(-\alpha n\eta_0)c_{0,x}}{c_0-\rho_{\mathrm{s}}},$$
$$\hat{D}_2 = \frac{\exp(-\alpha n\eta_0)}{c_0-\rho_{\mathrm{s}}}, \quad \hat{D}_3 = -\alpha_3 n. \qquad [40]$$

Because the unit normal at the cathode is in the opposite direction from that at the anode, the signs of the expressions involving $\hat{n}$ at the cathode are opposite to that at the anode. Hence, the boundary conditions at the cathode at $x = h_0^{\mathrm{c}}$ are given by

$$-c_{0,t}h_1^{\mathrm{c}} - D\left[c_1' + z\left(c_0\phi_1' + \phi_{0,x}c_1\right)\right] = 0, \qquad [41]$$

$$\beta_{\mathrm{v}} j_{0,0}\left(\hat{G}_1 h_1^{\mathrm{c}} + \hat{G}_2 c_1 + \hat{G}_3\phi_1\right) = -\omega h_1^{\mathrm{c}}, \qquad [42]$$

$$\begin{aligned}\beta_{\mathrm{m}}[&(D-D_+)c_1' + z_+D_+\rho_{\mathrm{s}}\phi_1' \\ &- (z_+D_+ - zD)\left(c_0\phi_1' + \phi_{0,x}c_1\right)] = -\omega h_1^{\mathrm{c}},\end{aligned} \qquad [43]$$

where the $\hat{G}_1$, $\hat{G}_2$ and $\hat{G}_3$ parameters are

$$\hat{G}_1 = \alpha_3 n\left(-\phi_{0,x} - \frac{\gamma k^2}{n}\right) + \frac{\exp(-\alpha n\eta_0)c_{0,x}}{c_0-\rho_{\mathrm{s}}},$$
$$\hat{G}_2 = \frac{\exp(-\alpha n\eta_0)}{c_0-\rho_{\mathrm{s}}}, \quad \hat{G}_3 = -\alpha_3 n. \qquad [44]$$

The capillary number $\mathrm{Ca} = \gamma$ appears in the $\hat{D}_1$ and $\hat{G}_1$ parameters in the form of γk^2, which is the source of the surface stabilizing effect that arises from the surface energy penalty incurred in creating additional surface area. The competition between this surface stabilizing effect and the surface destabilizing effect arising from the c_0, $c_{0,x}$ and $\phi_{0,x}$ fields sets the scale for the critical wavenumber k_{c}, which is the wavenumber at which the perturbation growth rate ω is 0 and the electrode surface is marginally stable.

***Discretization of perturbed state.*—**Without making further approximations, the equations for the perturbed state do not admit analytical solutions, thus we have to resort to numerical methods to solve them. To do so, the equations for the perturbed state are spatially discretized over a uniform grid with N grid points and a grid spacing $\Delta x = \frac{1}{N-1}$ using second-order accurate finite differences.[190] Details of this discretization process are provided in Section IV of Supplementary Material. In summary, the discretized equations can be written as a generalized eigenvalue problem given by

$$Yv = \omega Zv,$$
$$v = \left[\, h_1^{\mathrm{a}}\ c_{1,1}\ \phi_{1,1}\ c_{1,2}\ \phi_{1,2}\ \cdots\ c_{1,N-1}\ \phi_{1,N-1}\ c_{1,N}\ \phi_{1,N}\ h_1^{\mathrm{c}}\,\right]^{\mathrm{T}}, \qquad [45]$$

where $Y, Z \in \mathbb{R}^{(2N+2)\times(2N+2)}$, $v \in \mathbb{C}^{2N+2}$, $\omega \in \mathbb{C}$ and the second subscript in $c_{1,i}$ and $\phi_{1,i}$ for $i = 1, 2, \ldots, N$ denotes the grid point index. In the context of a generalized eigenvalue problem, the eigenvector v consists of the complex-valued amplitudes c_1, ϕ_1, h_1^{a} and h_1^{c} evaluated at the grid points, and the eigenvalue is the complex-valued growth rate ω. Although Y is non-singular, the time-independent terms in the equations for the perturbed state introduce rows of zeros in Z, therefore Z is singular and the generalized eigenvalue problem cannot be reduced to a standard eigenvalue problem. Specifically, Y is non-singular with rank $2N+2$ while Z is singular with rank N, and the total number of eigenvalues is $2N+2$.

Because Z is singular with rank N, there are N finite eigenvalues and $N+2$ infinite eigenvalues. This mathematical property is not always consistently noted in past literature on linear stability analysis of electrodeposition, although Sundström and Bark did mention that N different eigenvalues are obtained with N grid points that give rise to $2N+2$ equations without explicitly stating that the other $N+2$ eigenvalues are infinite.[149] The infinite eigenvalues are physically irrelevant to the linear stability analysis,[191,192] therefore we would want to focus on solving for the finite eigenvalues. This can be achieved by mapping the infinite eigenvalues to other arbitrarily chosen points in the complex plane via simple matrix transformations.[193] Details of how these transformations are performed are given in Section IV of Supplementary Material. There are methods for directly removing the infinite eigenvalues such as the "reduced" method[191,194,195] but they are more intrusive and require more extensive matrix manipulations as compared to the mapping technique[193] that we use.

The modified generalized eigenvalue problem that results from these transformations can then be solved using any eigenvalue solver. For linear stability analysis, we only need to find the eigenvalue with the largest real part instead of all the finite eigenvalues. Since the time complexity of finding all the eigenvalues typically scales as $\mathcal{O}\left(N^3\right)$ while that for finding $k \leq N$ of them, where $k = 1$ in our case, scales as $\mathcal{O}\left(kN^2\right)$, the computational cost is dramatically reduced by a factor of $\mathcal{O}(N)$ if we use an eigenvalue solver that can find subsets of eigenvalues and eigenvectors such as MATLAB's `eigs` solver.

***Numerical implementation.*—**The equations for the time-dependent base state in Base state section are numerically solved using the finite element method in COMSOL Multiphysics 5.3a. The eigenvalue with the largest real part and its corresponding eigenvector from the generalized eigenvalue problem for the perturbed state in Discretization of perturbed state section are then solved for using the `eigs` function in MATLAB R2018a. When the `eigs` function occasionally fails to converge for small values of the wavenumber k, we use Rostami and Xue's eigenvalue solver based on the matrix exponential,[196,197] which is more robust than the `eigs` function. The colormaps used for some of the plots in Results section are obtained from BrewerMap,[198] which is a MATLAB program available in the MATLAB File Exchange that implements the ColorBrewer colormaps.[199]

Results

Because of the large number of dimensionless parameters present, the parameter space is too immense to be explored thoroughly in this paper. Instead, the key dimensionless parameters that we focus on and vary are ρ_{s}, Da and J_{a} under galvanostatic conditions. $\rho_{\mathrm{s}} = 0$ corresponds to the classical case of an uncharged nanoporous medium while $\rho_{\mathrm{s}} \neq 0$ allows us to depart from this classical case and study its effects on the linear stability of the electrode surface. Experimentally, ρ_{s} can be tuned via layer-by-layer deposition of polyelectrolytes[180,200,201] or tethered immobilized anions.[76] Da is very sensitive to the specific reactions considered and varies significantly in practice. We focus on galvanostatic conditions instead of potentiostatic conditions because when an overlimiting current $J_{\mathrm{a}} > 1$ is applied on a classical system with $\rho_{\mathrm{s}} = 0$, as discussed in Transport section, the Sand's time t_{s} provides a time scale at which the electric field at the cathode diverges that causes the perturbation growth rate to diverge too. This allows us to focus the linear stability analysis on times immediately before, at and immediately after t_{s}.

For the results discussed in Convergence analysis, Parameter sweeps, Comparison between numerical and approximate solutions and Pulse electroplating and pulse charging sections below, we assume the following dimensional quantities for a typical electrolyte in a typical nanoporous medium: $T = 298$ K, $M_{\mathrm{m}} = 6.941$ g/mol (arbitrarily

Table II. Dimensionless parameters that are used for results in Convergence analysis, Parameter sweeps, Comparison between numerical and approximate solutions and Pulse electroplating and pulse charging sections for a typical electrolyte in a typical nanoporous medium.

Dimensionless parameter	Description	Value
ν_+	Number of cations formed from complete dissolution of 1 molecule of neutral salt	1
ν	Number of anions formed from complete dissolution of 1 molecule of neutral salt	1
z_+	Cation charge number	1
z	Anion charge number	-1
D_+	Cation diffusivity	1
D	Anion diffusivity	1
n	Number of electrons transferred in charge transfer reaction	1
α	Charge transfer coefficient	0.5
$\mathrm{Ca} = \gamma$	Capillary number, ratio of capillary constant to inter-electrode distance (Equation 22)	8.74×10^{-5}
β_m	Ratio of atomic volume of solid metal to reciprocal electrolyte concentration	1.30×10^{-4}
β_D	Weighted ratio of cation and anion diffusivities	0.25
β_v	Ratio of β_m to β_D	5.20×10^{-4}
ξ_+	Ratio of electrolyte concentration to standard cation concentration	0.01
$E^\ominus$	Standard electrode potential	0
L_y	Aspect ratio in y direction	100
L_z	Aspect ratio in z direction	100
ρ_s	Ratio of background charge density to electrolyte concentration	$-1, -0.75, -0.5, -0.25, -0.05, 0, 0.05$
Da	Damköhler number, ratio of reaction rate to diffusion rate (Equation 14)	0.1, 1, 10

pick lithium metal),[202] $\rho_\mathrm{m} = 0.534\,\mathrm{g/cm^3}$ (arbitrarily pick lithium metal),[202] $L_x = 60\,\mu\mathrm{m}$, $L_y = L_z = 100L_x = 6\,\mathrm{mm}$ ($L_x \ll L_y = L_z$ to model a thin gap cell that reduces effects of gravity-induced convection (buoyancy)[150]), $c_0 = 10\,\mathrm{mM}$ (note that c_0 here is the dimensional initial neutral salt bulk concentration, not the dimensionless base state anion concentration), $c_+^\ominus = 1\,\mathrm{M} = 10^3\,\mathrm{mol/m^3}$ (standard concentration) and $\gamma = 1\,\mathrm{J/m^2}$ (typical surface energy of metal/electrolyte interface).[149] Corresponding to these dimensional quantities, all dimensionless parameters that are used for the results in Convergence analysis, Parameter sweeps, Comparison between numerical and approximate solutions and Pulse electroplating and pulse charging sections are given in Table II.

Approximations.—At the heart of the linear stability analysis is the competition between the destabilizing effect that arises from the amplification of surface protrusions by diffusive fluxes in a positive feedback loop and the stabilizing effect that arises from the surface energy penalty incurred in the creation of additional surface area. Therefore, in the dispersion relation $\omega(k)$, we expect to see some local maxima or possibly just a single global maximum, which we denote as $\{k_\mathrm{max}, \omega_\mathrm{max}\}$, where the electrode surface is maximally unstable. We also expect to see a critical wavenumber k_c corresponding to $\omega = 0$ where the electrode surface is marginally stable. When k is larger than k_c, ω is always negative because the surface energy stabilizing effect always dominates when the wavenumber is sufficiently large. We note that k_c is always greater than k_max. Corresponding to k_max and k_c are the maximum wavelength $\lambda_\mathrm{max} = \frac{2\pi}{k_\mathrm{max}}$ and critical wavelength $\lambda_\mathrm{c} = \frac{2\pi}{k_\mathrm{c}}$ respectively. In a porous medium, the characteristic pore size $h_\mathrm{c} = 2d_\mathrm{p}$, where d_p is the pore diameter, sets a threshold or cutoff for overall electrode surface stabilization: we should observe stabilization if h_c is smaller than λ_c.[158] If h_c is larger than λ_c, then the most unstable eigenmode dominates the electrode surface growth with a growth rate of ω_max and the characteristic length scale of this instability is λ_max. Therefore, $\{k_\mathrm{max}, \omega_\mathrm{max}\}$ and k_c are the most physically informative points of the dispersion relation. We now derive an approximation for the dispersion relation $\omega(k)$ that is valid at high values of k relative to k_c and will be useful for computing $\{k_\mathrm{max}, \omega_\mathrm{max}\}$ and k_c quickly and accurately because k_max and k_c tend to be large. The approximation is also useful for verifying the full numerical solution at high k, which will be discussed in Convergence analysis section.

When k is sufficiently large compared to k_c, at the cathode at $x = h_0^\mathrm{c} = 1$, we expect $k^2 c_1$ to balance c_1'', and $k^2\phi_1$ to balance ϕ_1'' in Equations 35 and 36 respectively. Therefore, k^{-2} is a small parameter multiplying the highest order spatial derivative terms c_1'' and ϕ_1'', and the spatial profiles for c_1 and ϕ_1 form a boundary layer with characteristic thickness k^{-1}. Hence, as an ansatz for the boundary layer analysis, we assume

$$c_1 = A\exp[k(x-1)], \quad \phi_1 = B\exp[k(x-1)], \qquad [46]$$

where A and B are arbitrary constants that are determined from the boundary conditions at $x = h_0^\mathrm{c} = 1$. By assuming such an ansatz, the cathode is effectively decoupled from the anode and the perturbation growth rate is entirely dependent on the boundary conditions at the cathode. The validity of this ansatz is corroborated by our observations that $h_1^\mathrm{c} \gg h_1^\mathrm{a}$ generally in our numerical simulations, especially at large values of k, which was also observed by Sundström and Bark.[149] Imposing the boundary conditions at $x = h_0^\mathrm{c} = 1$, we obtain

$$\xi_1(k) = \frac{c_{0,t}}{zc_0Dk}, \quad \xi_2(k) = -\frac{z\phi_{0,x}+k}{zc_0k}, \quad B(k) = -\xi_1h_1 + \xi_2A, \qquad [47]$$

$$A(k) = -\frac{\beta_\mathrm{v}j_{0,0}\left(\hat{G}_1 - \xi_1\hat{G}_3\right) - \beta_\mathrm{m}\alpha_5\xi_1k}{\beta_\mathrm{v}j_{0,0}\left(\hat{G}_2 + \xi_2\hat{G}_3\right) - \beta_\mathrm{m}\left[(\alpha_1 - \alpha_5\xi_2)k - \alpha_2\phi_{0,x}\right]}h_1, \qquad [48]$$

$$\omega(k) = \beta_\mathrm{m}\left\{\frac{\left[(\alpha_1 - \alpha_5\xi_2)k - \alpha_2\phi_{0,x}\right]\left[\beta_\mathrm{v}j_{0,0}\left(\hat{G}_1 - \xi_1\hat{G}_3\right) - \beta_\mathrm{m}\alpha_5\xi_1k\right]}{\beta_\mathrm{v}j_{0,0}\left(\hat{G}_2 + \xi_2\hat{G}_3\right) - \beta_\mathrm{m}\left[(\alpha_1 - \alpha_5\xi_2)k - \alpha_2\phi_{0,x}\right]} - \alpha_5\xi_1k\right\}, \qquad [49]$$

where we define $\alpha_1 = D - D_+$, $\alpha_2 = z_+D_+ - zD$ and $\alpha_5 = \alpha_2c_0 - z_+D_+\rho_\mathrm{s}$ for brevity.

Approximate values of $\{k_\mathrm{max}, \omega_\mathrm{max}\}$ can be obtained by solving $\omega'(k) = 0$ and requiring $\omega''(k) < 0$ where the primes indicate total derivatives with respect to k. In addition, by solving $\omega(k) = 0$, we can obtain approximate values of k_c. However, this process is tedious because the first term inside the braces in Equation 49 is a rational function that consists of polynomials in k of relatively high degrees. Specifically, after multiplying the numerator and denominator of this term by k, it becomes a rational function with a numerator that is a polynomial in k of degree 4 and a denominator that is a polynomial in k of degree 2. Therefore, for the purpose of quickly approximating $\{k_\mathrm{max}, \omega_\mathrm{max}\}$ and k_c, we first find a simpler and yet still accurate analytical approximation for k_c, which can then used as an initial guess for numerically solving for $\{k_\mathrm{max}, \omega_\mathrm{max}\}$ using Equation 49 with MATLAB's `fminbnd` optimizer. Such an approximation can be obtained by assuming k_c is large enough that $\hat{G}_2c_1 \ll \hat{G}_1h_1$ and $\hat{G}_3\phi_1 \ll \hat{G}_1h_1$

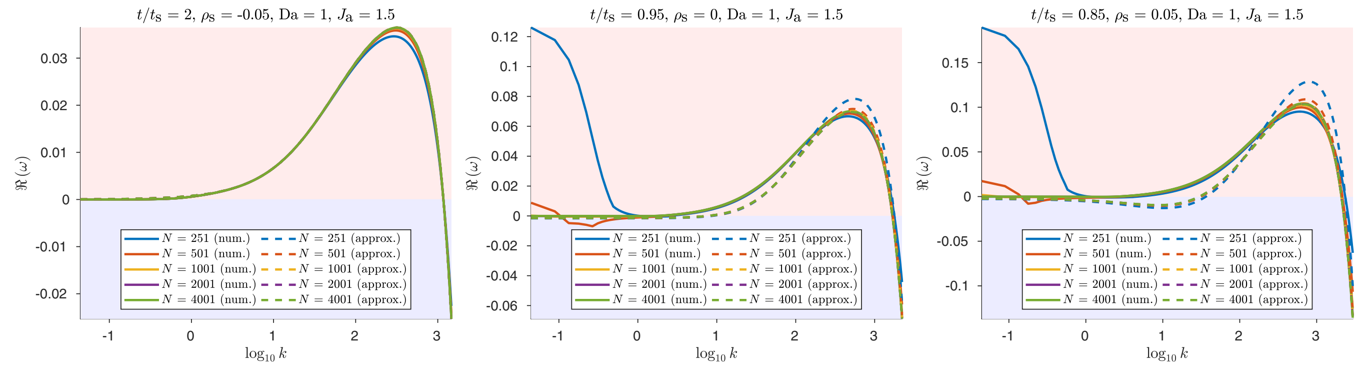

Figure 2. Convergence plots of $\Re(\omega)$ against $\log_{10} k$ with Da = 1 and J_a = 1.5 (overlimiting current) for $\rho_s \in \{-0.05, 0, 0.05\}$ and $N \in \{251, 501, 1001, 2001, 4001\}$ used in convergence analysis. The $\frac{t}{t_s}$ values to which the curves correspond are indicated in the figure titles. In the legends, "num." refers to numerical solutions while "approx." refers to approximate solutions.

and then setting $\omega = 0$ in Equation 42, thus resulting in

$$k_c = \left\{ \frac{1}{\alpha_3 \gamma} \left[-\alpha_3 n \phi_{0,x} + \frac{\exp(-\alpha n \eta_0) c_{0,x}}{c_0 - \rho_s} \right] \right\}^{\frac{1}{2}}. \qquad [50]$$

We observe that k_c scales as $\mathrm{Ca}^{-\frac{1}{2}} = \gamma^{-\frac{1}{2}}$, which is expected because the surface energy stabilizing effect appears in the form of γk^2 in $\hat{G}_1$ in Equation 42, and this scaling agrees with that obtained in previous work done on linear stability analysis of electrodeposition.[149,150,158,164,203]

Convergence analysis.—Before analyzing the physical significance of the linear stability analysis results, we would want to first establish the accuracy and convergence of the full numerical solution of the dispersion relation $\omega(k)$. To this end, we perform a numerical convergence analysis in which we examine the convergence of the numerical solution as the number of grid points N increases. At the same time, we also compute the approximate $\omega(k)$ given by Equation 49 because we expect the numerical and approximate solutions to agree well at high values of k; this therefore provides another way of checking the accuracies of both the numerical and approximate solutions.

To demonstrate how the numerical dispersion relation $\omega(k)$ changes with N, we fix Da = 1 and J_a = 1.5 (overlimiting current) and plot numerically computed $\Re(\omega)$ against $\log_{10} k$ for $\rho_s \in \{-0.05, 0, 0.05\}$ and $N \in \{251, 501, 1001, 2001, 4001\}$ at specific $\frac{t}{t_s}$ values in Figure 2. As expected, the numerical solutions converge quickly as N increases from 251 to 4001. For $\rho_s = 0$ and $\rho_s = 0.05$ at small values of k, when the value of N is small at 251 or 501, we observe that there are anomalously large values of $\Re(\omega)$ that vanish at larger values of N. This is because when N is too small, the grid is not sufficiently fine to accurately resolve the base state variables, in particular the rapidly increasing electric field at the cathode near t_s, thus leading to an overestimation of the destabilizing effect caused by electrodiffusion and an underestimation of the stabilizing effect caused by surface energy. The numerical and approximate solutions also expectedly agree well with each other at large values of k and this agreement improves as N increases, thus confirming that the approximations are accurate at high k.

Because we are mostly interested in the $k_{\max}$, $\omega_{\max}$ and k_c points on the $\omega(k)$ curve, we plot them against N in Figure 3. We observe that the numerically computed $k_{\max}$, $\omega_{\max}$ and k_c curves rapidly level off and converge to constant values as N increases. The numerical and approximate solutions also agree very well as N increases, which is expected because $k_{\max}$ and k_c are large and the approximations are accurate at high k. As a compromise between numerical accuracy and computational time, we pick N = 1001 for all numerical and approximate solutions computed in the following sections.

Parameter sweeps.—The base state anion concentration field c_0, electrolyte electric potential field ϕ_0 and electric field $E_0 = -\phi_{0,x}$ possess salient features that are useful for understanding the linear stability analysis results. We focus on galvanostatic conditions under an overlimiting current $J_a > 1$ because as explained in Transport section, doing so provides us with Sand's time t_s as a time scale at which the bulk electrolyte is depleted at the cathode. Depending on the sign of ρ_s, the c_0, ϕ_0 and E_0 fields behave differently at $t = t_s$ and beyond. Fixing Da = 1 and J_a = 1.5 (overlimiting current), we plot c_0, ϕ_0 and E_0 against x for various $\frac{t}{t_s}$ values for $\rho_s \in \{-0.05, 0, 0.05\}$ in Figure 4. For $\rho_s = -0.05$, because the system can go beyond t_s and eventually reach a steady state, we show plots up to $t = 2t_s$. For $\rho_s = 0$, since ϕ_0 and E_0 at the cathode diverge at t_s, which cause the numerical solver to stop converging, we can only show plots up to $t = 0.95t_s$. For $\rho_s = 0.05$, because $\rho_s > 0$ effectively reduces t_s as discussed in Transport section, we show plots up to $t = 0.85t_s$.

For $\rho_s = -0.05 < 0$, the distinguishing features of running the system at an overlimiting current carried by surface conduction are the anion depletion region at the cathode and the bounded and constant electric field E_0 in this depletion region after $t = t_s$. Because the anion concentration gradient almost vanishes in the depletion region, the current in this region is predominantly not carried by electrodiffusion but by electromigration of the counterions in the electric double layers (EDLs) under the aforementioned bounded and constant electric field E_0, i.e., surface conduction. Moreover, because of this additional surface conductivity, when compared to $\rho_s = 0$ and $\rho_s = 0.05$, E_0 is always smaller at all x for a given t. On the other hand, for the classical case of $\rho_s = 0$, E_0 at the cathode quickly increases near t_s and eventually diverges at t_s. Relative to this classical case, for $\rho_s = 0.05 > 0$, E_0 is always greater at all x for a given t and eventually diverges at the cathode earlier than t_s because of the "negative" surface conductivity conferred by the positive background charge as discussed in Transport section.

We now examine the dispersion relation $\omega(k)$ by plotting numerically computed $\Re(\omega)$ against k for various $\frac{t}{t_s}$ values for $\rho_s \in \{-0.05, 0, 0.05\}$, Da $\in \{0.1, 1, 10\}$ and J_a = 1.5 (overlimiting current) in Figure 5. In Figure 5, ρ_s increases from left to right and Da increases from bottom to top. Generally for all the parameters considered, the ω curve, in particular the $k_{\max}$, $\omega_{\max}$ and k_c points, increases and "moves in the northeast direction" as t increases; qualitatively, the "total amount of instability" increases with t. For $\rho_s = -0.05 < 0$, when compared to $\rho_s = 0$ and $\rho_s = 0.05$, the ω curve is the smallest at a given t because of a smaller base state electric field E_0. The ω curve also remains bounded at all t and eventually reaches a steady state that is almost attained near $t = 2t_s$ because E_0 at the cathode behaves in the same fashion. In sharp contrast, for the classical case of $\rho_s = 0$ near t_s, the ω curve grows dramatically because of the rapidly increasing E_0 at the cathode, which eventually diverges at t_s and in turn causes the ω curve to diverge at t_s too. Compared to this classical case, for

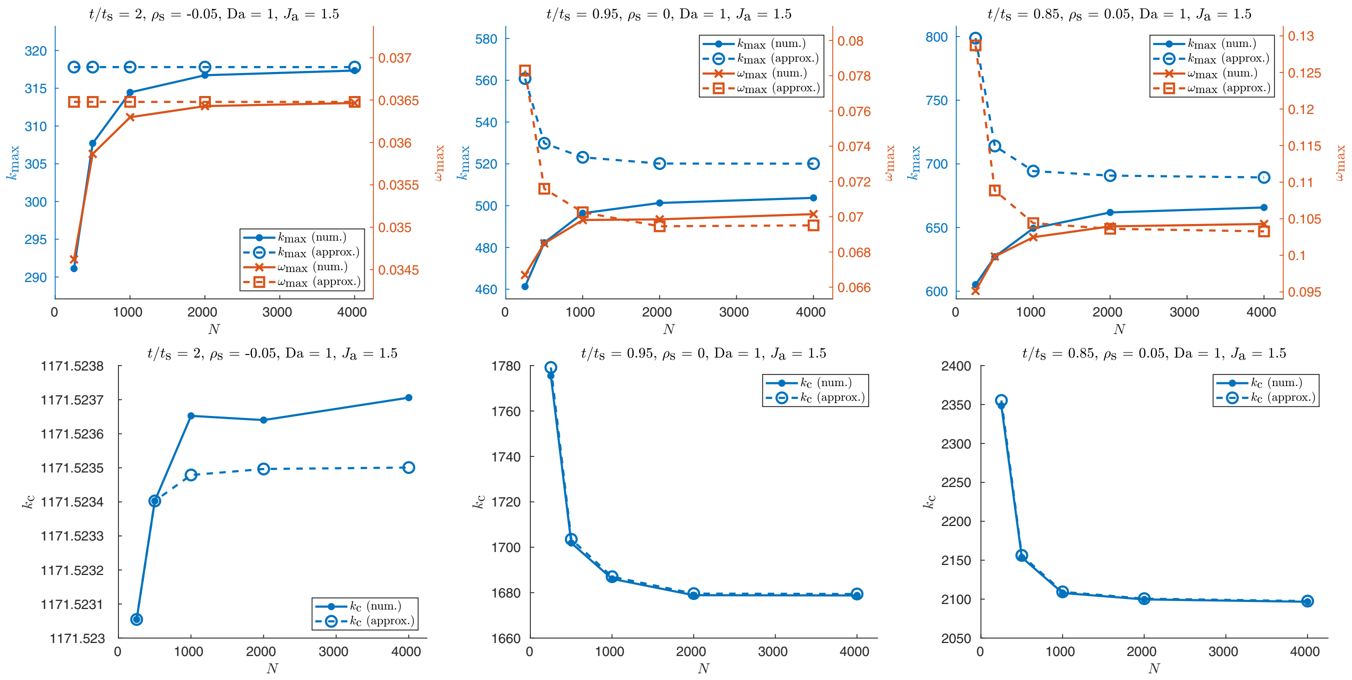

Figure 3. Convergence plots of $k_{\max}$, $\omega_{\max}$ and k_c against N with $\mathrm{Da} = 1$ and $J_a = 1.5$ (overlimiting current) for $\rho_s \in \{-0.05, 0, 0.05\}$ used in convergence analysis. Top row: Convergence plots of $k_{\max}$ and $\omega_{\max}$. Bottom row: Convergence plots of k_c. The $\frac{t}{t_s}$ values to which the curves correspond are indicated in the figure titles. In the legends, "num." refers to numerical solutions while "approx." refers to approximate solutions.

$\rho_s = 0.05 > 0$, because E_0 at the cathode is larger at a given t and diverges earlier than t_s, the ω curve accordingly grows even more rapidly at earlier times and diverges earlier than t_s. Therefore, by bounding the electric field at the cathode, the presence of a negative background charge confers additional stabilization to the system beyond what is provided by surface energy effects, although it does not completely stabilize the system as there are still regions of positive growth rate in the dispersion relation. On the other hand, for the classical case of zero background charge, the system rapidly destabilizes near Sand's time and ultimately diverges at Sand's time because of the diverging electric field at the cathode, which is also demonstrated in Ref. 150. Relative to this classical case, the presence of a positive background charge destabilizes the system even further by generating an electric field at the cathode that is larger at a given time and diverges earlier than Sand's time, resulting in higher growth rates at earlier times and in finite time divergence earlier than Sand's time.

We observe that increasing Da generally increases ω but this effect is very insignificant because the application of an overlimiting current implies that the system is always diffusion-limited regardless of what Da is. Hence, in this regime of diffusion-limited electrodeposition under an overlimiting current, specific details of the electrochemical reaction kinetics model are not important in influencing the dispersion relation as long as the model includes the surface energy stabilizing effect, which typically occurs in the functional form of γk^2.

In the interest of space, plots of numerically computed $\Re(\omega)$ against k for $J_a = 1$ (limiting current) and $J_a = 0.5$ (underlimiting current) are not shown here but are given in Figures 1 and 2 in Section V of Supplementary Material respectively. Since the system is still always diffusion-limited for $J_a = 1$, the trends observed for $J_a = 1$ are qualitatively similar to our previous discussion for $J_a = 1.5$, except that the ω values are smaller because a smaller applied current density results in a smaller electric field at the cathode. For $J_a = 0.5$, because the applied current density is underlimiting, Sand's time is not defined and at the cathode, the bulk electrolyte concentration does not vanish and the electric field does not diverge at any t. Therefore, the ω curve remains bounded at all t and reaches a steady state eventually. Moreover, ω generally increases with Da, and this increase is especially pronounced when Da increases from 1 to 10; this effect was also observed by Sundström and Bark[149] who focused their analysis on underlimiting currents. This increase in ω is not directly caused by E_0 because E_0 does not change appreciably despite the increase in Da (refer to Figures 3 to 5 in Section VI of Supplementary Material). Rather, as discussed in Electrochemical reaction kinetics section, the system becomes diffusion-limited when $\mathrm{Da} \gg 1$, causing the surface perturbations to destabilize faster.

As discussed in Approximations section, at each t point, each ω curve exhibits a global maximum $\{k_{\max}, \omega_{\max}\}$ and a critical wavenumber k_c, which is where the curve crosses the horizontal axis $\omega = 0$. The $\{k_{\max}, \omega_{\max}\}$ and k_c points provide a succinct way to summarize the most physically significant features of the $\omega(k)$ curve for all the parameter ranges we have explored thus far. Therefore, for $\rho_s \in \{-0.05, 0, 0.05\}$, $\mathrm{Da} \in \{0.1, 1, 10\}$ and $J_a \in \{0.5, 1, 1.5\}$, we plot numerically computed $k_{\max}$ and $\omega_{\max}$ against $\frac{t}{t_s}$ in Figure 6 and numerically computed k_c against $\frac{t}{t_s}$ in Figure 7. For $J_a \geq 1$, we observe that the $k_{\max}$ and $\omega_{\max}$ curves diverge near t_s for $\rho_s \geq 0$ but level off to constant values past t_s for $\rho_s < 0$, therefore these curves appear as if they are "fanning out". In contrast, for $J_a < 1$, the $k_{\max}$ and $\omega_{\max}$ curves level off past t_s for all values of ρ_s as the system eventually reaches a steady state when an underlimiting current is applied. The k_c curves have the same qualitative shape as the $k_{\max}$ curves except that they are larger, as expected. The effects of Da and J_a on the $k_{\max}$, $\omega_{\max}$ and k_c values, which are previously discussed in the context of the dispersion relation, are also clearly reflected in Figures 6 and 7.

In an effort to make the electrode surface less unstable at overlimiting current, we focus on $\rho_s < 0$ to determine how much additional stabilization a negative ρ_s confers to the surface as it gets increasingly more negative. Subsequently, we plot numerically computed $k_{\max}$, $\omega_{\max}$ and k_c against $\frac{t}{t_s}$ for $\rho_s \in \{-1, -0.75, -0.5, -0.25, -0.05\}$, $\mathrm{Da} = 1$ and $J_a = 1.5$ in Figure 8. While a more negative ρ_s generally decreases $k_{\max}$, $\omega_{\max}$ and k_c, it is clear that there are diminishing returns to the amount of additional stabilization achieved. It also appears that complete stabilization is not possible as $\omega_{\max}$ remains posi-

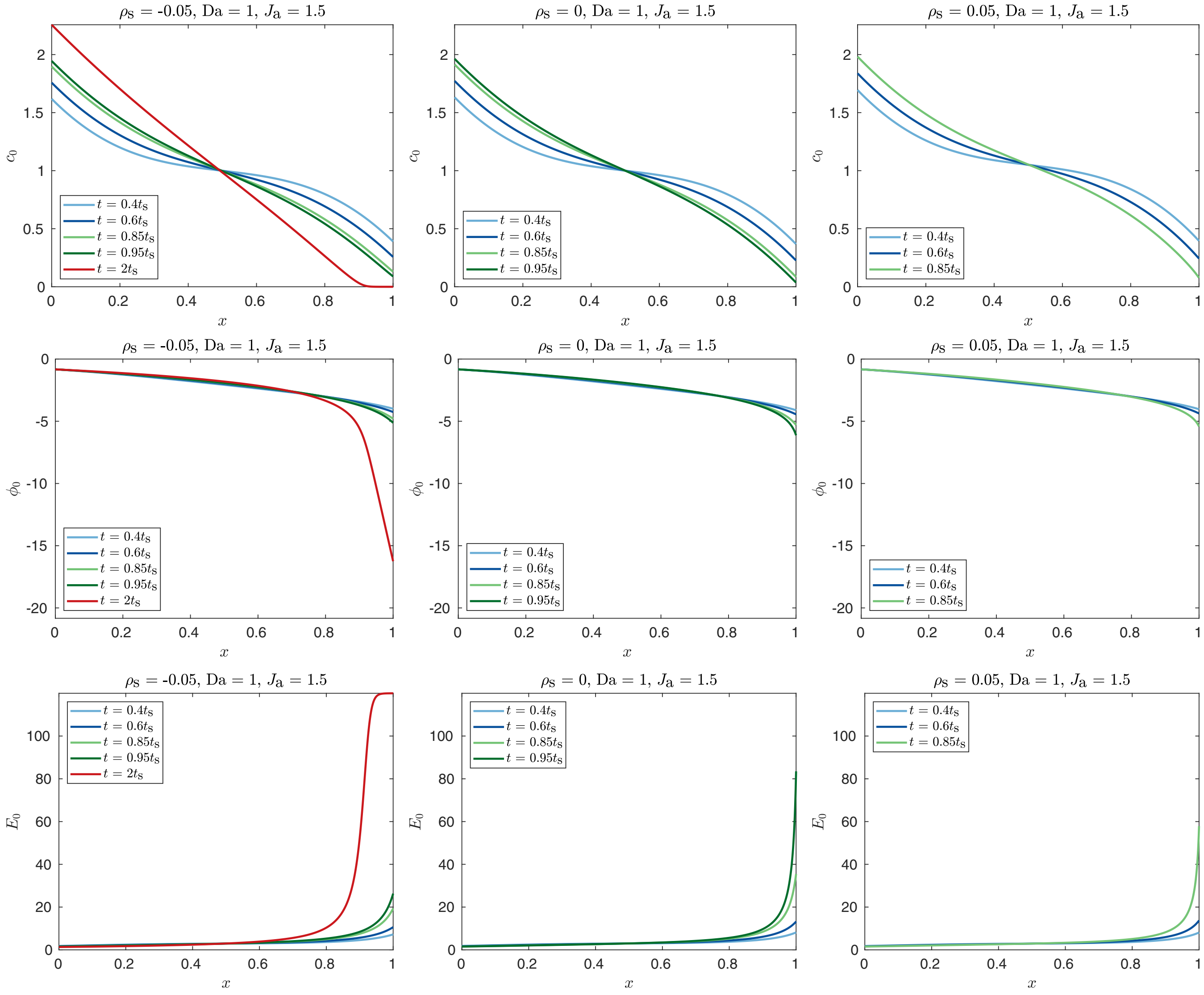

Figure 4. Plots of dimensionless base state anion concentration c_0, electrolyte electric potential ϕ_0 and electric field E_0 against x for various $\frac{t}{t_s}$ values with $\mathrm{Da} = 1$ and $J_a = 1.5$ (overlimiting current) for $\rho_s \in \{-0.05, 0, 0.05\}$. First row: Plots of c_0 against x. Second row: Plots of ϕ_0 against x. Third row: Plots of E_0 against x. Blue lines correspond to early times $t = 0.4t_s$ and $t = 0.6t_s$, green lines correspond to times near Sand's time $t = 0.85t_s$ and $t = 0.95t_s$, and red line corresponds to time beyond Sand's time $t = 2t_s$. For each color, intensity increases in the direction of increasing t.

tive even for $\rho_s = -1$, albeit at a small value. In practice, it is probable that a sufficiently small and positive $\omega_{\max}$ value can be deemed to be small enough for considering an electrode surface "practically stable", but experiments that measure and correlate $\omega_{\max}$ with observations of metal growth need to be performed in order to determine this threshold $\omega_{\max}$ value.

Comparison between numerical and approximate solutions.—To illustrate how well the approximations given by Equations 49 and 50 work for the parameter ranges considered, we plot numerical and approximate values of $k_{\max}$, $\omega_{\max}$ and k_c against $\frac{t}{t_s}$ for $\rho_s \in \{-0.05, 0, 0.05\}$, $\mathrm{Da} = 1$ and $J_a = 1.5$ in Figure 9. In the interest of space, these plots for other values of Da and J_a are provided in Figures 6 to 11 of Section VII of Supplementary Material. For all parameter ranges considered, the agreement between numerical and approximate values of $k_{\max}$, $\omega_{\max}$ and k_c is excellent, giving us confidence that the approximations are useful for rapidly and accurately computing $k_{\max}$, $\omega_{\max}$ and k_c. This confirms that $k_{\max}$ and k_c are large enough that Equations 49 and 50, which have assumed that k is sufficiently large, are accurate for approximating them. We will therefore use Equations 49 and 50 extensively in Application to copper electrodeposition and Pulse electroplating and pulse charging sections that follow.

Application to copper electrodeposition.—We now apply linear stability analysis to the specific case of copper electrodeposition and electrodissolution and compare it with experimental data[180] to determine how well theory agrees with experiment. Because copper electrodeposition involves the overall transfer of two electrons that are transferred one at a time in a serial manner, we need to first derive the overall expression for the faradaic current density J_F.

Assuming that the activity of electrons is 1 and dilute solution theory is applicable, for a n-electron transfer reaction, the dimensionless forms of Equations 12 and 9 are given by

$$\begin{aligned} J_F &= j_0\{\exp(-\alpha n\eta) - \exp[(1-\alpha)n\eta]\}, \\ j_0 &= k_0 n \hat{c}_O^{1-\alpha}\hat{c}_R^{\alpha} = \mathrm{Da}\, n \hat{c}_O^{1-\alpha}\hat{c}_R^{\alpha}, \end{aligned} \qquad [51]$$

$$\Delta\phi^{eq} = \frac{1}{n}\ln\frac{\hat{c}_O}{\hat{c}_R} + E^{\ominus} - \frac{2\gamma\mathscr{H}}{n}. \qquad [52]$$

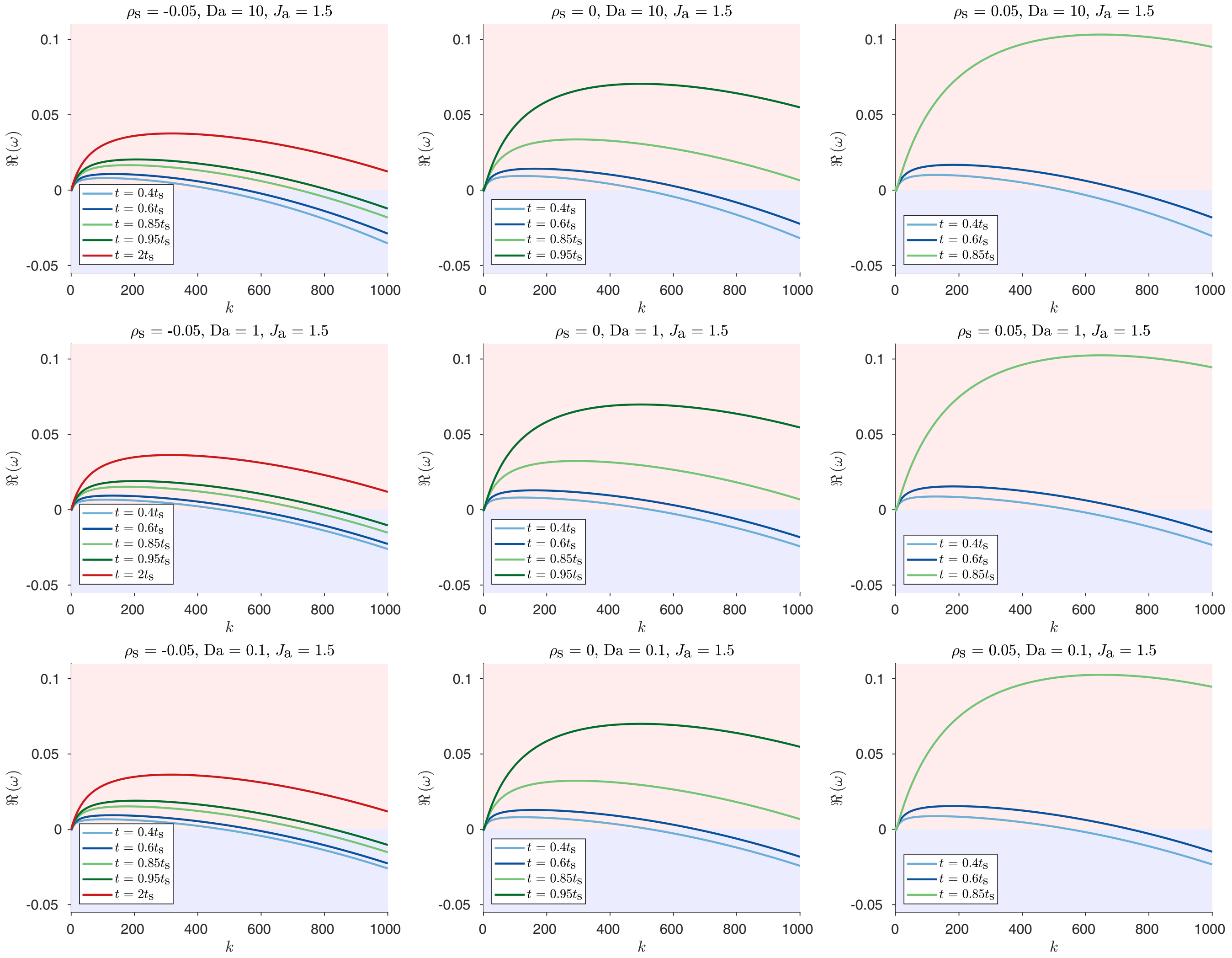

Figure 5. Plots of numerical $\Re(\omega)$ against k for various $\frac{t}{t_s}$ values for $\rho_s \in \{-0.05, 0, 0.05\}$, Da $\in \{0.1, 1, 10\}$ and $J_a = 1.5$ (overlimiting current). ρ_s increases from left to right and Da increases from bottom to top. Blue lines correspond to early times $t = 0.4t_s$ and $t = 0.6t_s$, green lines correspond to times near Sand's time $t = 0.85t_s$ and $t = 0.95t_s$, and red line corresponds to time beyond Sand's time $t = 2t_s$. For each color, intensity increases in the direction of increasing t.

For multistep electron transfer reactions, it is more convenient to work with $\Delta\phi$ instead of η. Therefore, we rewrite J_F in terms of $\Delta\phi$ as

$$J_F = n\left\{k_c\hat{c}_O \exp\left[-\alpha n\left(\Delta\phi + \frac{2\gamma\mathscr{H}}{n}\right)\right] - k_a\hat{c}_R \exp\left[(1-\alpha)n\left(\Delta\phi + \frac{2\gamma\mathscr{H}}{n}\right)\right]\right\}, \qquad [53]$$

$$E^\ominus = \frac{1}{n}\ln\frac{k_c}{k_a}, \quad k_0 = k_a^\alpha k_c^{1-\alpha}, \qquad [54]$$

where k_c and k_a are the cathodic and anodic rate constants respectively.

The reaction mechanism for copper electrodeposition and electrodissolution is given by[103,204–206]

$$\mathrm{Cu^{2+}(aq) + e^- \rightleftharpoons Cu^+(ads)}, \qquad [55]$$

$$\mathrm{Cu^+(ads) + e^- \rightleftharpoons Cu(s)}, \qquad [56]$$

where (aq), (ads) and (s) indicate aqueous, adsorbed and solid respectively. The first step is assumed to be the rate-determining step while the second step is assumed to be at equilibrium. Applying Equation 53 to each step, noting that the activity of solid metal is 1 and rewriting J_F in terms of η, we obtain

$$J_F = j_0\{\exp(-\alpha_1\eta) - \exp[(2-\alpha_1)\eta]\},$$
$$j_0 = 2k_0\hat{c}_+^{1-\frac{\alpha_1}{2}} = 2\mathrm{Da}\hat{c}_+^{1-\frac{\alpha_1}{2}}, \qquad [57]$$

$$\Delta\phi^{eq} = \frac{1}{2}\ln\hat{c}_+ + E^\ominus - 2\gamma\mathscr{H}, \qquad [58]$$

where α_1 is the charge transfer coefficient of the first step.

Previously in Electrochemical reaction kinetics section, for a 1-step n-electron transfer metal electrodeposition reaction, the dimensionless forms of Equations 12 and 13 are given by

$$J_F = j_0\{\exp(-\alpha n\eta) - \exp[(1-\alpha)n\eta]\}, \quad j_0 = k_0 n\hat{c}_+^{1-\alpha} = \mathrm{Da}n\hat{c}_+^{1-\alpha}, \qquad [59]$$

$$\Delta\phi^{eq} = \frac{1}{n}\ln\hat{c}_+ + E^\ominus - \frac{2\gamma\mathscr{H}}{n}. \qquad [60]$$

By comparing Equations 57 and 58 with Equations 59 and 60, we set $n = 2$ and $\alpha = \frac{\alpha_1}{2}$ and replace γ with 2γ in the original set of equations in order to adapt the linear stability analysis for copper electrodeposition.

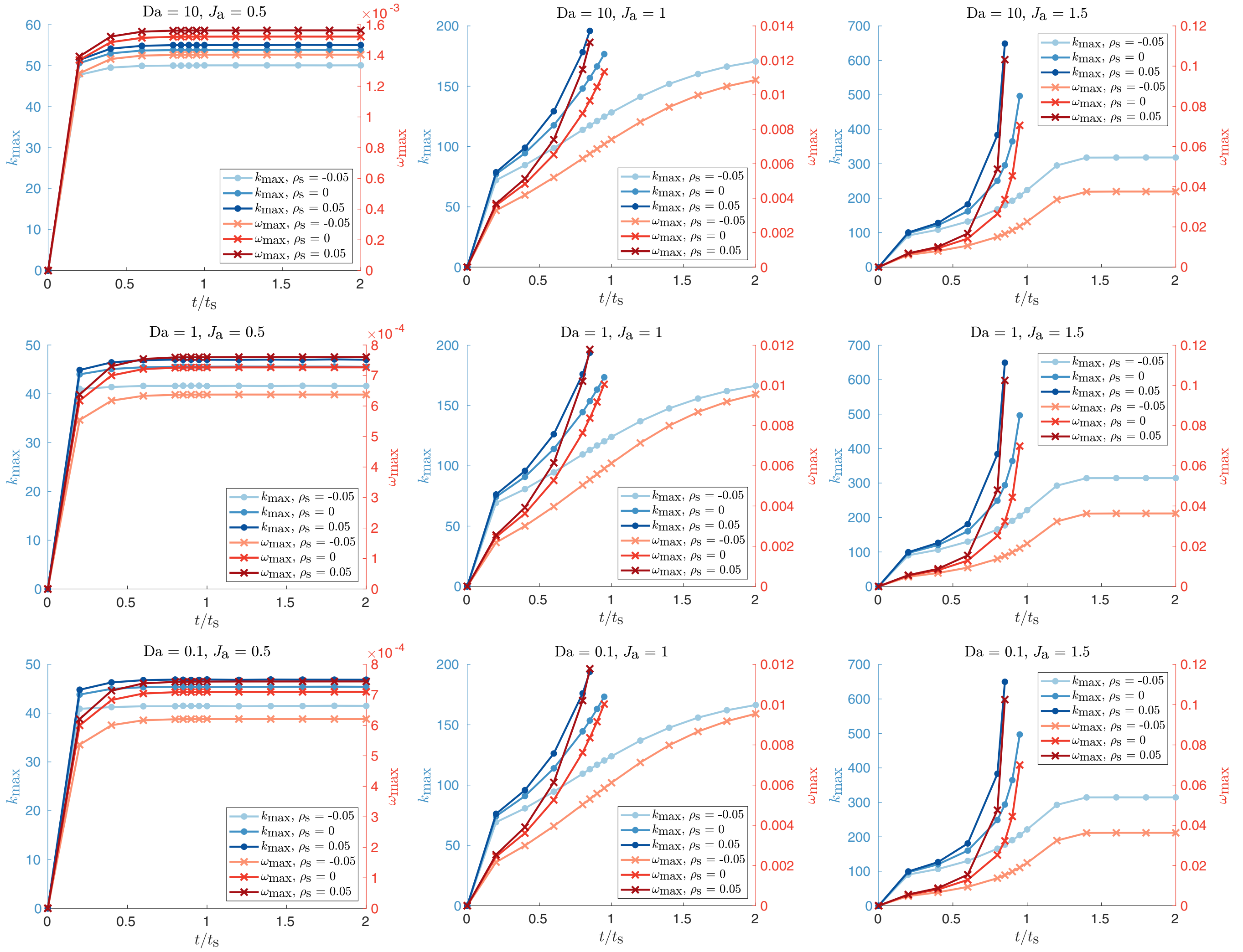

Figure 6. Plots of numerical $k_{\max}$ and $\omega_{\max}$ against $\frac{t}{t_s}$ for $\rho_s \in \{-0.05, 0, 0.05\}$, Da $\in \{0.1, 1, 10\}$ and $J_a \in \{0.5, 1, 1.5\}$. ρ_s increases from left to right and Da increases from bottom to top.

By carrying out nonlinear least squares fitting on experimental steady state current-voltage relations, we have previously performed parameter estimation[181] for copper electrodeposition in a copper(II) sulfate ($CuSO_4$) electrolyte in cellulose nitrate (CN) membranes,[180] which are a random nanoporous medium with well connected pores. The parameters that are estimated are ρ_s, τ, Da, α_1 and ϵ_p and their fitted values are provided in Table III in Ref. 181. Other parameters specific to the copper electrodeposition reaction, $CuSO_4$ electrolyte and CN membranes used are also provided in Tables I and II in Ref. 181. For the surface energy of the copper/electrolyte interface, we use dimensional $\gamma = 1.85\,\mathrm{J/m^2}$ given in Table I in Ref. 164.

For our analysis here, the specific experimental datasets that we focus on are labeled $CN_2(-)$ and $CN_2(+)$ in Ref. 181, which correspond to negatively and positively charged CN membranes respectively with a dimensional electrolyte concentration c_0 of 100 mM. We will drop the 2 subscript for brevity. The morphologies of the electrodeposited copper films, which are visualized by EDS (energy dispersive X-ray spectroscopy) maps, for these CN(−) and CN(+) membranes at 2000 s for dimensional applied currents I_a of 15 mA, 20 mA and 25 mA are given in Figure 10a that consists of magnifications of EDS maps taken from Figures 6a to 6f of Ref. 180. At 15 mA, the copper films for both CN(+) and CN(−) membranes appear to be uniform and stable. However, at 20 mA and 25 mA, the film for CN(+) becomes very unstable and roughens more as the applied current increases. It is difficult to determine quantitatively the instability wavelength using the relatively low resolution EDS maps but it is probably much smaller than 5 μm. In contrast, for CN(−), the film still remains uniform and stable at 20 mA but slightly destabilizes and roughens at 25 mA with an instability wavelength probably on the order of 5 μm. In summary, the onset of overall electrode surface destabilization occurs at 20 mA for CN(+) with an instability wavelength of much smaller than 5 μm and at 25 mA for CN(−) with an instability wavelength of about 5 μm.

Because the EDS maps are taken at 2000 s, which is much longer than the diffusion times for CN(−) and CN(+) of 41.8 s and 40.9 s respectively, we assume that the system is at steady state. This assumption allows us to use the semi-analytical expressions for the base state variables in Ref. 181, which we have previously discussed in Base state section, to compute approximate values of $\{k_{\max}, \omega_{\max}\}$ and k_c using Equations 49 and 50. The CN(−) dataset has a dimensional limiting current of 18.2 mA while the CN(+) dataset has a dimensional maximum current, which we have discussed in Transport section, of 16.9 mA. Therefore, for CN(−), the three applied currents of 15 mA, 20 mA and 25 mA correspond to underlimiting, slightly overlimiting and overlimiting currents respectively. On the other hand, for CN(+), the model eventually diverges and does not admit a steady state when the applied current I_a is above the maximum current $I_{\max}$, therefore we can only obtain finite values of $\{k_{\max}, \omega_{\max}\}$ and k_c for the applied current of 15 mA while the model predicts infinite values of $\{k_{\max}, \omega_{\max}\}$ and k_c for the applied currents of 20 mA and 25 mA due to finite time divergence of the system. Other fitted key dimensionless parameters

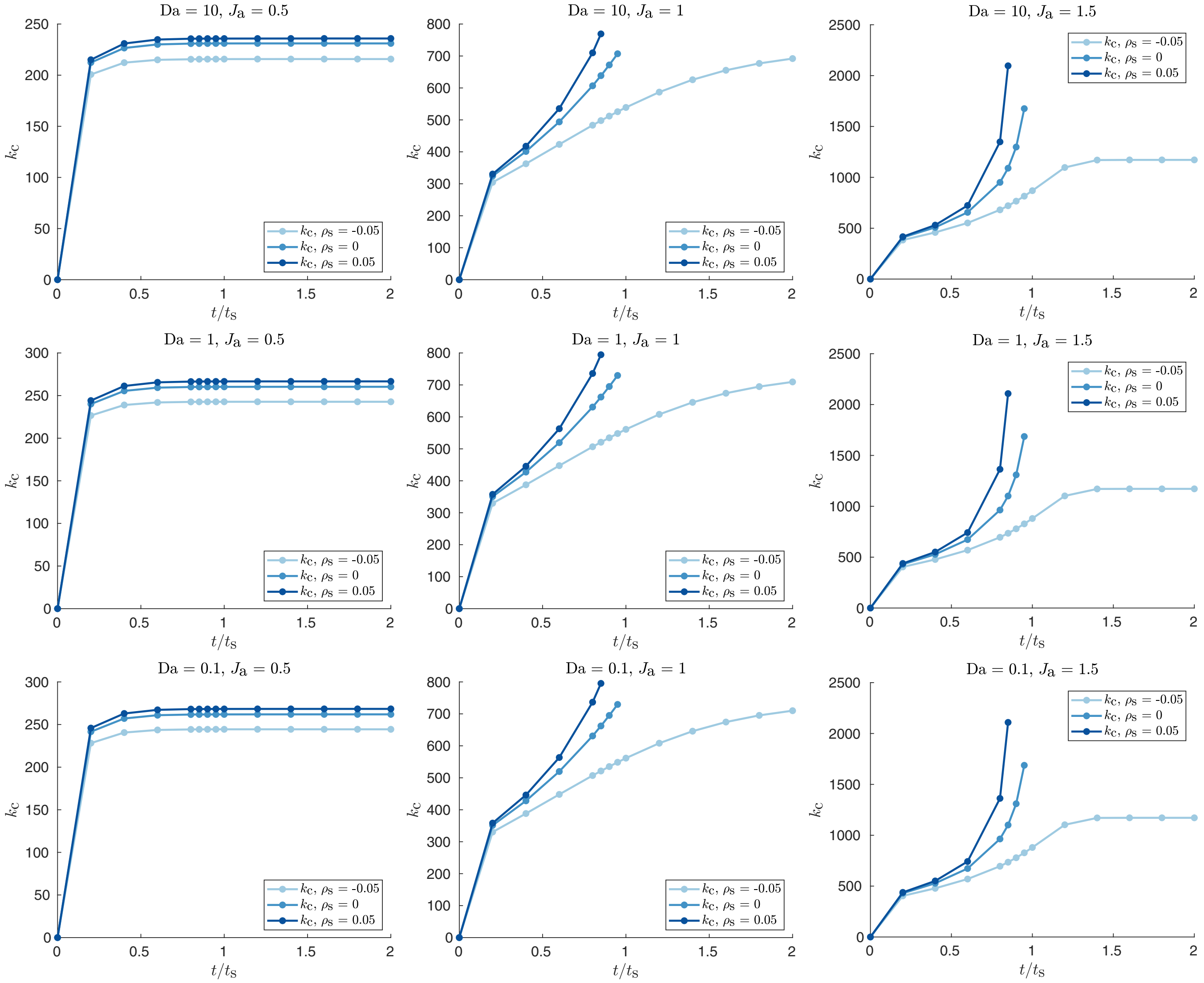

Figure 7. Plots of numerical k_c against $\frac{t}{t_s}$ for $\rho_s \in \{-0.05, 0, 0.05\}$, $\mathrm{Da} \in \{0.1, 1, 10\}$ and $J_a \in \{0.5, 1, 1.5\}$. ρ_s increases from left to right and Da increases from bottom to top.

include $\rho_s \approx -0.01$ and $\mathrm{Da} \approx 2.50$ for CN(−) and $\rho_s \approx 0.236$ and $\mathrm{Da} \approx 0.473$ for CN(+).

To summarize the model predictions, we plot approximate dimensional values of λ_c and $\lambda_{\max}$ against the dimensional applied current I_a in Figure 10. In the λ_c plot in Figure 10a, we also indicate the characteristic pore size h_c of $0.5 \pm 0.1\,\mu\mathrm{m}$, which is given by twice the pore diameter d_p of $250 \pm 50\,\mathrm{nm}$,[180] in order to determine if the model predicts overall electrode surface stabilization. As discussed in Approximations section, we expect overall electrode surface stabilization if $h_c < \lambda_c$, which corresponds to the blue shaded region in the λ_c plot.

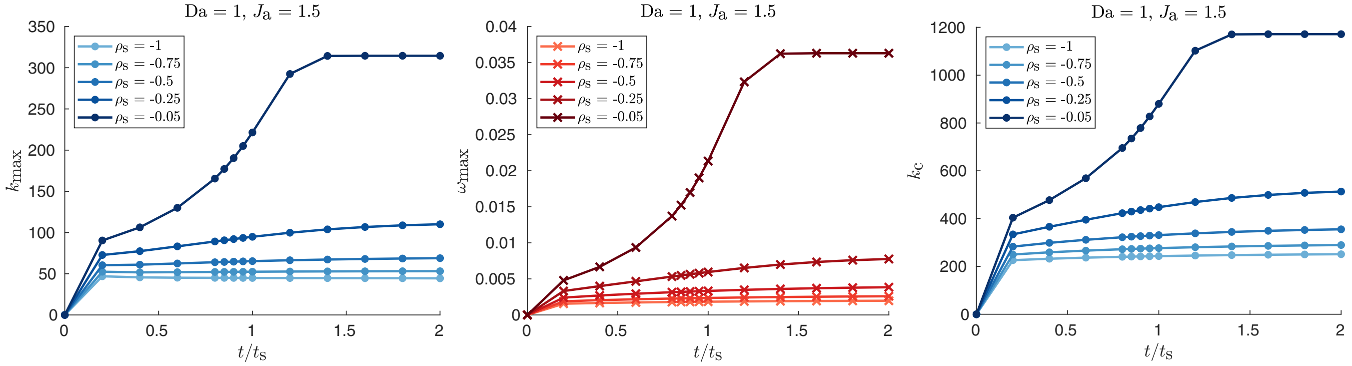

Figure 8. Plots of numerical $k_{\max}$, $\omega_{\max}$ and k_c against $\frac{t}{t_s}$ for $\rho_s \in \{-1, -0.75, -0.5, -0.25, -0.05\}$, Da = 1 and J_a = 1.5 (overlimiting current) for investigating additional stabilization of electrode surface conferred by increasingly negative ρ_s values.

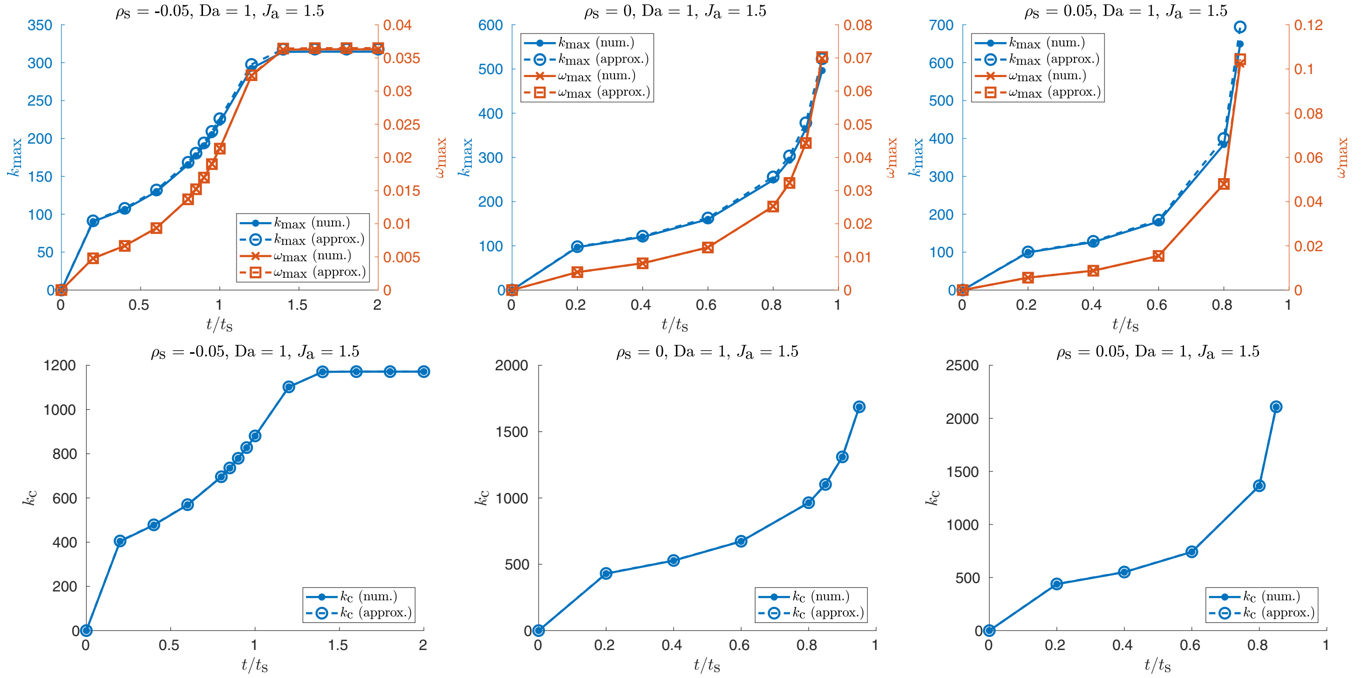

Figure 9. Plots of numerical and approximate values of $k_{\max}$, $\omega_{\max}$ and k_c against $\frac{t}{t_s}$ for $\rho_s \in \{-0.05, 0, 0.05\}$, Da = 1 and $J_a = 1.5$ (overlimiting current). Top row: Plots of $k_{\max}$ and $\omega_{\max}$. Bottom row: Plots of k_c. In the legends, "num." refers to numerical solutions while "approx." refers to approximate solutions.

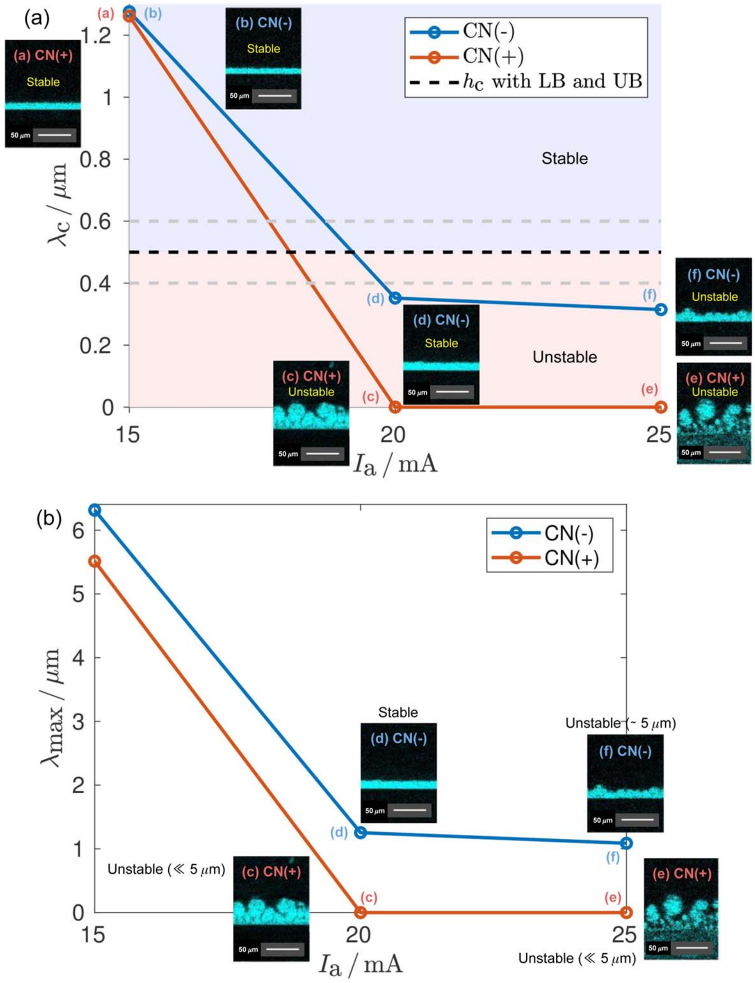

Figure 10. Plots of EDS (energy dispersive X-ray spectroscopy) maps at 2000 s, and approximate dimensional λ_c (a) and $\lambda_{\max}$ (b) at steady state against dimensional applied current I_a for copper electrodeposition in 100 mM copper(II) sulfate ($CuSO_4$) electrolyte in cellulose nitrate (CN) membranes. EDS maps in (a) and (b) are magnifications of EDS maps in Figures 6a to 6f of Ref. 180 where the scale bars indicate 50 µm. $h_c = 0.5 \pm 0.1$ µm in the λ_c plot in (a) is the characteristic pore size where the mean is indicated by the black dashed line while the lower (LB) and upper (UB) bounds are indicated by gray dashed lines.

On the contrary, we expect overall electrode surface destabilization if $h_c > \lambda_c$, which corresponds to the red shaded region in the λ_c plot, and the characteristic instability wavelength is $\lambda_{\max}$. Comparing the λ_c plot with our previous discussion of the onset of overall electrode surface destabilization suggested by the copper film morphologies observed experimentally, we see that the model generally agrees well with experiment; the only disagreement is at $I_a = 20\,\text{mA}$ where the model predicts destabilization for CN(−), which has $\lambda_c = 0.352\,\mu\text{m}$, while the EDS map of the copper film at this applied current shows that the film appears to be stable. Nonetheless, this disagreement in theory and experiment is relatively minor since $\lambda_c = 0.352\,\mu\text{m}$ for CN(−) at $I_a = 20\,\text{mA}$ is only slightly smaller than the mean of h_c of $0.5\,\mu\text{m}$ and is almost equal to the lower bound of h_c of $0.4\,\mu\text{m}$. In addition, the model predicts $\lambda_{\max} = 0$ (because $k_{\max} \to \infty$ when $I_a > I_{\max}$) at $I_a = 20\,\text{mA}$ and $I_a = 25\,\text{mA}$ for CN(+) while it predicts $\lambda_{\max} = 1.09\,\mu\text{m}$ at $I_a = 25\,\text{mA}$ for CN(−). These model predictions of $\lambda_{\max}$ qualitatively agree well with the experimentally observed instability wavelengths at these applied currents that we have previously discussed. Therefore, in conclusion, the theory agrees reasonably well with experimental data, especially given that many assumptions and simplifications are made in the model.

Pulse electroplating and pulse charging.—For many electrochemical applications such as electroplating and charging of metal batteries, which is equivalent to electrodeposition at the metal negative electrode, it is desirable to operate them as quickly as possible at a high current without causing the formation of dendrites that short-circuit the system. To delay or prevent the formation of dendrites, it is common to perform pulse electroplating of metals[207,208] or pulse charging of lithium metal batteries (LMBs) and lithium-ion batteries (LIBs)[209–217] so that there is sufficient time between pulses for the concentration gradients and electric field in the system to relax. For pulse electroplating of metals, it has been empirically observed that the crystal grain size generally decreases with applied current.[207,208] Using an applied direct current to perform silver electrodeposition under galvanostatic conditions, Aogaki experimentally observed that the crystal grain size decreases with time,[137,138] which agrees well with theoretical predictions from linear stability analysis previously done by Aogaki and Makino.[136] With all these considerations in mind, we apply our linear stability analysis with a time-dependent base state as a tool to investigate how pulse electroplating protocols with high average applied currents, which are inherently time-dependent, affect the linear stability of the electrode surface and the crystal grain size for both zero and negative pore surface charges.

Based on the results in Application to copper electrodeposition section, we generally expect the characteristic pore size h_c to be larger than the critical wavelength λ_c at high applied currents, therefore the electrode surface is unstable with a characteristic instability wavelength $\lambda_{\max}$. Because a pulse current is applied, $\lambda_{\max}$ varies in time and hence, it would be useful to define an average $\lambda_{\max}$ that averages out the effect of time. In this spirit, we define the average maximum wavenumber $\bar{k}_{\max}$ and the corresponding average maximum wavelength $\bar{\lambda}_{\max}$ as

$$\bar{k}_{\max} = \frac{\int_0^{t_f} k_{\max}\omega_{\max}\,\mathrm{d}t}{\int_0^{t_f} \omega_{\max}\,\mathrm{d}t}, \quad \bar{\lambda}_{\max} = \frac{2\pi}{\bar{k}_{\max}}, \qquad [61]$$

where t_f is the final time of the pulse and each maximum wavenumber $k_{\max}$ is weighted by its corresponding maximum growth rate $\omega_{\max}$. We expect $\bar{\lambda}_{\max}$ to be on the same order of magnitude as the the crystal grain size that is observed experimentally. As a simple example, we suppose that the pulse electroplating protocol is a periodic pulse wave J_a with an "on" (charging) time of Δt_{on}, a "off" (relaxation) time of Δt_{off}, and a period T given by $T = \Delta t_{on} + \Delta t_{off}$. The duty cycle γ_{dc} is given by $\gamma_{dc} = \frac{\Delta t_{on}}{T}$ and the average applied current density $\bar{J}_a$ over one period is given by $\bar{J}_a = J_{a,p}\gamma_{dc}$ where $J_{a,p}$ is the peak applied current density. Hence, for a particular $\bar{J}_a$, a smaller γ_{dc} implies a larger $J_{a,p}$.

For the classical case of $\rho_s = 0$, we pick $\bar{J}_a = 1$ and $\Delta t_{on} = 0.0125 t_s$ and vary γ_{dc} from 0.2 to 1 (direct current) where the Sand's time t_s is calculated based on $\bar{J}_a$. $\bar{J}_a$, Δt_{on} and γ_{dc} should be carefully chosen such that $J_{a,p}$ is not too high to deplete the bulk electrolyte at the cathode during the "on" cycle so that the system does not diverge at any point in time; this explains why $\gamma_{dc} < 0.2$ for our choice of $\bar{J}_a = 1$ and $\Delta t_{on} = 0.0125 t_s$ cannot be numerically simulated. For $\rho_s = -0.05$, we pick $\bar{J}_a = 1.5$ and $\Delta t_{on} = t_s$ and vary γ_{dc} from 0.1 to 1 (direct current) to drive the system at an overlimiting average applied current density. We also fix Da = 1 for both cases and use Equations 49 and 50 to compute approximate values of $k_{\max}$ and $\omega_{\max}$. For these choices of parameters, as an illustrative example, we plot J_a, approximate $k_{\max}$ and approximate $\omega_{\max}$ against t for $\gamma_{dc} = 0.5$ in Figure 11. We note that the large overshoot in $k_{\max}$ at the beginning of each "on" cycle for $\rho_s = 0$ is caused by the sharp rate of increase of the concentration gradients and electric field as J_a rapidly increases from 0 in the "off" cycle to $J_{a,p}$ in the "on" cycle. Corresponding to these pulse waves, we plot $\bar{\lambda}_{\max}$ against γ_{dc} in Figure 12. For both $\rho_s = 0$ and $\rho_s = -0.05$, $\bar{\lambda}_{\max}$ increases with γ_{dc}, which agrees with the empirical observation that the crystal grain size generally decreases with applied current.[207,208] The ability to experimentally impart a negative pore surface charge to the nanoporous medium therefore enables pulse electroplating at overlimiting currents for electrodepositing a large amount of charge at a high rate and tuning the desired crystal grain size.

Conclusions

We have derived the full model that couples the leaky membrane model for ion transport, which is capable of predicting overlimiting current due to surface conduction, with Butler-Volmer reaction kinetics, which describes the metal electrodeposition reaction, and performed linear stability analysis on it with respect to a time-dependent base state. The volume-averaged background charge density can generally be of any sign. As a result, we have generalized previous work on linear stability analysis of electrodeposition carried out in Refs. 149,150,158. We then performed a boundary layer analysis on the perturbed state in order to derive an accurate approximation for the dispersion relation and a convergence analysis to verify the accuracy and convergence of the full numerical solution of the dispersion relation. By performing parameter sweeps over the volume-averaged background charge density, Damköhler number and applied current density under galvanostatic conditions, we have concluded that a negative background charge significantly stabilizes the electrode surface instability, although it does not completely stabilize it, while a positive background charge further destabilizes this instability. We have also verified that the approximations for the maximum wavenumber, maximum growth rate and and critical wavenumber are very accurate, and applied them to demonstrate good agreement between theory and experimental data for copper electrodeposition in cellulose nitrate membranes.[180] Lastly, we have employed the linear stability analysis as a tool to analyze the dependence of the crystal grain size on duty cycle in pulse electroplating. These results demonstrate the predictive power and robustness of the theory despite its simplicity. Although detailed analysis of the Poisson-Nernst-Planck-Stokes equations for transport in a microchannel by Nielsen and Bruus[134] reveals that the leaky membrane model for surface conduction is at best a rough approximation of the real system, the good agreement between theory and experiment that we have demonstrated suggests that the model is applicable in similar electrochemical systems using charged membranes such as shock electrodeposition for information storage applications[218] and shock electrodialysis for water treatment.[111–113]

We have made many assumptions and simplifications in the model presented, and relaxing some of them offers opportunities for extending it in useful ways. First, we have ignored surface adsorption, surface diffusion of adsorbed species[139–142] and additional mechanical effects such as pressure, viscous stress and deformational stress,[156,157,159,161–163] which confer additional stabilization to the electrode surface. Adding these physics and chemistry to the model are likely to result in finite values of the maximum wavenumber, maximum growth rate and critical wavenumber near and at Sand's time under an overlimiting current for zero and positive background charges respectively, as opposed to diverging in our current model. The inclusion of

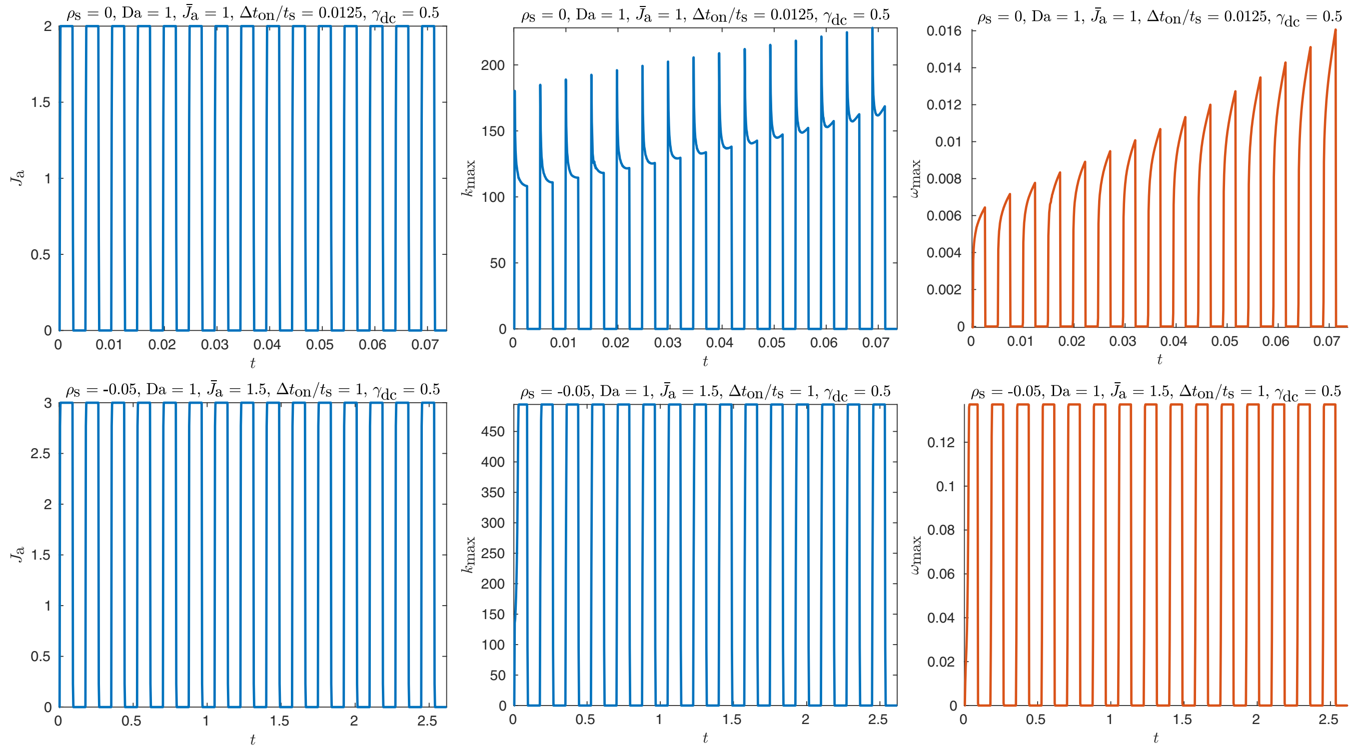

Figure 11. Plots of J_a, approximate k_{max} and approximate ω_{max} against t with Da = 1 and $\gamma_{dc} = 0.5$ for pulse electroplating. Top row: $\rho_s = 0$, $\bar{J}_a = 1$ and $\Delta t_{on} = 0.0125 t_s$. Bottom row: $\rho_s = -0.05$, $\bar{J}_a = 1.5$ and $\Delta t_{on} = t_s$.

these additional mechanical effects will also extend the applicability of the model to solid electrolytes[219] that are used in solid state batteries. Deformation of the porous medium caused by metal growth inside the pores also results in a porosity that varies in both time and space whose effects would be interesting to study. Second, in order to apply the linear stability analysis to lithium metal batteries (LMBs), we would also need to model the solid electrolyte interphase (SEI) layer,[176–179] which will certainly increase the complexity of the model but also make it more predictive. Incorporating these two aforementioned extensions into the model may help explain recent experimental studies of lithium growth that have demonstrated that competing SEI reactions and stress effects lead to root growth before Sand's time or below limiting current,[93–95] which is different from tip growth of dendrites under transport limitation that we have focused on in this paper. Third, other chemical mechanisms for overlimiting current such as water splitting[114,115] and current-induced membrane discharge[132] may be present. These effects are typically highly nonlinear and therefore, we expect them to significantly influence the transient base state and linear stability analysis. Fourth, we should consider the effects of coupling nucleation, which is fundamentally a nonlinear instability unlike spinodal decomposition that is a linear instability, to the current model. Specifically, nucleation may affect the transient base state dur-

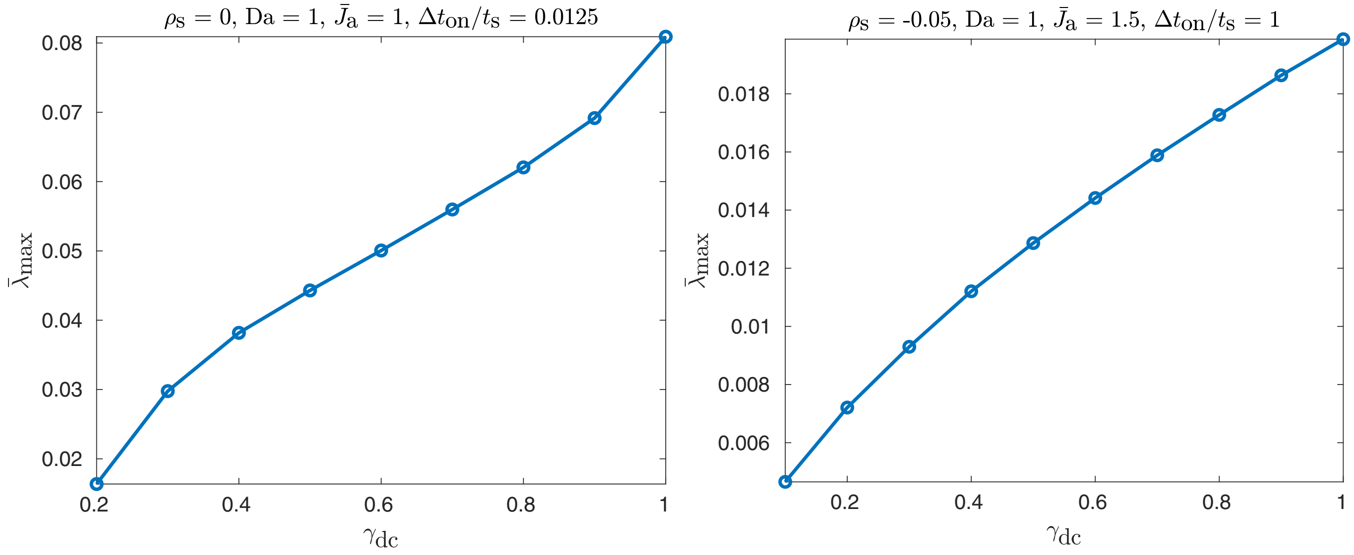

Figure 12. Plots of $\bar{\lambda}_{max}$ against γ_{dc} with Da = 1. Left: $\rho_s = 0$, $\bar{J}_a = 1$ and $\Delta t_{on} = 0.0125 t_s$. Right: $\rho_s = -0.05$, $\bar{J}_a = 1.5$ and $\Delta t_{on} = t_s$.

ing initial and early reaction-limited surface growth and create surface roughness on the scale of the characteristic nucleus size, which may in turn influence overall electrode surface stabilization or destabilization when the system reaches transport limitation near or at Sand's time. Fifth, an interesting and useful generalization of the reaction model would be to use the symmetric Marcus-Hush-Chidsey kinetics[220,221] or asymmetric Marcus-Hush kinetics[222] instead of Butler-Volmer kinetics for modeling electron transfer reactions, which would afford us the reorganization energy as a key system parameter whose influence on the linear stability of the electrode surface can be investigated.

Acknowledgments

E. Khoo acknowledges support from the National Science Scholarship (PhD) funded by Agency for Science, Technology and Research, Singapore (A*STAR). H. Zhao and M. Z. Bazant acknowledge support from the Toyota Research Institute through the D3BATT Center on Data-Driven-Design of Rechargeable Batteries.

ORCID

Edwin Khoo https://orcid.org/0000-0002-3171-7982
Hongbo Zhao https://orcid.org/0000-0002-0932-0719
Martin Z. Bazant https://orcid.org/0000-0002-8200-4501

References

1. J. S. Langer, *Reviews of Modern Physics*, **52**, 1 (1980).
2. D. A. Kessler, J. Koplik, and H. Levine, *Advances in Physics*, **37**, 255 (1988).
3. M. C. Cross and P. C. Hohenberg, *Reviews of Modern Physics*, **65**, 851 (1993).
4. W. M. Orr, *Proceedings of the Royal Irish Academy. Section A: Mathematical and Physical Sciences*, **27**, 9 (1907).
5. W. M. Orr, *Proceedings of the Royal Irish Academy. Section A: Mathematical and Physical Sciences*, **27**, 69 (1907).
6. A. Sommerfeld, *Atti del*, **4**, 116 (1908).
7. S. A. Orszag, *Journal of Fluid Mechanics*, **50**, 689 (1971).
8. B. Zaltzman and I. Rubinstein, *Journal of Fluid Mechanics*, **579**, 173 (2007).
9. E. Ben-Jacob and P. Garik, *Nature*, **343**, 523 (1990).
10. L. Lopez-Tomas, J. Mach, P. P. Trigueros, F. Mas, J. Claret, and F. Sagues, *Chaos, Solitons & Fractals*, **6**, 287 (1995).
11. C. Léger, L. Servant, J. L. Bruneel, and F. Argoul, *Physica A: Statistical Mechanics and its Applications Proceedings of the 20th IUPAP International Conference on Statistical Physics*, **263**, 305 (1999).
12. F. Sagués, M. Q. López-Salvans, and J. Claret, *Physics Reports*, **337**, 97 (2000).
13. M. Rosso, E. Chassaing, V. Fleury, and J.-N. Chazalviel, *Journal of Electroanalytical Chemistry International Symposium on Materials Processing for Nanostructured Devices 2001*, **559**, 165 (2003).
14. W. Schwarzacher, *Journal of Physics: Condensed Matter*, **16**, R859 (2004).
15. M. Rosso, *Electrochimica Acta Electrochemical Processing of Tailored Materials Selection of papers from the 4th International Symposium (EPTM 2005) 3–5 October 2005, Kyoto, Japan*, **53**, 250 (2007).
16. A. M. Turing, *Phil. Trans. R. Soc. Lond. B*, **237**, 37 (1952).
17. P. G. Saffman and G. I. Taylor, *Proc. R. Soc. Lond. A*, **245**, 312 (1958).
18. P. G. Saffman, *Journal of Fluid Mechanics*, **173**, 73 (1986).
19. D. Bensimon, L. P. Kadanoff, S. Liang, B. I. Shraiman, and C. Tang, *Reviews of Modern Physics*, **58**, 977 (1986).
20. G. M. Homsy, *Annual Review of Fluid Mechanics*, **19**, 271 (1987).
21. M. Mirzadeh and M. Z. Bazant, *Physical Review Letters*, **119**, 174501 (2017).
22. W. W. Mullins and R. F. Sekerka, *Journal of Applied Physics*, **34**, 323 (1963).
23. W. W. Mullins and R. F. Sekerka, *Journal of Applied Physics*, **35**, 444 (1964).
24. R. F. Sekerka, *Journal of Applied Physics*, **36**, 264 (1965).
25. M. Z. Bazant, *Accounts of Chemical Research*, **46**, 1144 (2013).
26. M. Z. Bazant, *Faraday Discussions*, **199**, 423 (2017).
27. N. M. Schneider, J. H. Park, J. M. Grogan, D. A. Steingart, H. H. Bau, and F. M. Ross, *Nature Communications*, **8**, 2174 (2017).
28. T. A. Witten and L. M. Sander, *Physical Review Letters*, **47**, 1400 (1981).
29. T. A. Witten and L. M. Sander, *Physical Review B*, **27**, 5686 (1983).
30. P. Meakin, *Physical Review Letters*, **51**, 1119 (1983).
31. T. Vicsek, *Physical Review Letters*, **53**, 2281 (1984).
32. R. M. Brady and R. C. Ball, *Nature*, **309**, 225 (1984).
33. M. Matsushita, M. Sano, Y. Hayakawa, H. Honjo, and Y. Sawada, *Physical Review Letters*, **53**, 286 (1984).
34. E. Ben-Jacob, R. Godbey, N. D. Goldenfeld, J. Koplik, H. Levine, T. Mueller, and L. M. Sander, *Physical Review Letters*, **55**, 1315 (1985).
35. Y. Sawada, A. Dougherty, and J. P. Gollub, *Physical Review Letters*, **56**, 1260 (1986).
36. D. Grier, E. Ben-Jacob, R. Clarke, and L. M. Sander, *Physical Review Letters*, **56**, 1264 (1986).
37. P. P. Trigueros, J. Claret, F. Mas, and F. Sagués, *Journal of Electroanalytical Chemistry and Interfacial Electrochemistry*, **312**, 219 (1991).
38. J. Erlebacher, P. C. Searson, and K. Sieradzki, *Physical Review Letters*, **71**, 3311 (1993).
39. E. Ben-Jacob, G. Deutscher, P. Garik, N. D. Goldenfeld, and Y. Lareah, *Physical Review Letters*, **57**, 1903 (1986).
40. E. Ben-Jacob, P. Garik, and D. Grier, *Superlattices and Microstructures*, **3**, 599 (1987).
41. D. G. Grier, D. A. Kessler, and L. M. Sander, *Physical Review Letters*, **59**, 2315 (1987).
42. E. Ben-Jacob, P. Garik, T. Mueller, and D. Grier, *Physical Review A*, **38**, 1370 (1988).
43. P. Garik, D. Barkey, E. Ben-Jacob, E. Bochner, N. Broxholm, B. Miller, B. Orr, and R. Zamir, *Physical Review Letters*, **62**, 2703 (1989).
44. V. Fleury, M. Rosso, J.-N. Chazalviel, and B. Sapoval, *Physical Review A*, **44**, 6693 (1991).
45. J. Elezgaray, C. Léger, and F. Argoul, *Physical Review Letters*, **84**, 3129 (2000).
46. C. Léger, J. Elezgaray, and F. Argoul, *Physical Review E*, **61**, 5452 (2000).
47. E. Ben-Jacob, N. Goldenfeld, J. S. Langer, and G. Schön, *Physical Review Letters*, **51**, 1930 (1983).
48. E. Ben-Jacob, N. Goldenfeld, J. S. Langer, and G. Schön, *Physical Review A*, **29**, 330 (1984).
49. E. Ben-Jacob, N. Goldenfeld, B. G. Kotliar, and J. S. Langer, *Physical Review Letters*, **53**, 2110 (1984).
50. F. Argoul, E. Freysz, A. Kuhn, C. Léger, and L. Potin, *Physical Review E*, **53**, 1777 (1996).
51. C. Léger, J. Elezgaray, and F. Argoul, *Physical Review Letters*, **78**, 5010 (1997).
52. C. Léger, J. Elezgaray, and F. Argoul, *Physical Review E*, **58**, 7700 (1998).
53. C. Léger, F. Argoul, and M. Z. Bazant, *The Journal of Physical Chemistry B*, **103**, 5841 (1999).
54. C. Léger, J. Elezgaray, and F. Argoul, *Journal of Electroanalytical Chemistry*, **486**, 204 (2000).
55. M. Rosso, E. Chassaing, J. N. Chazalviel, and T. Gobron, *Electrochimica Acta*, **47**, 1267 (2002).
56. V. Fleury, J.-N. Chazalviel, and M. Rosso, *Physical Review Letters*, **68**, 2492 (1992).
57. V. Fleury, J.-N. Chazalviel, and M. Rosso, *Physical Review E*, **48**, 1279 (1993).
58. V. Fleury, J. H. Kaufman, and D. B. Hibbert, *Nature*, **367**, 435 (1994).
59. M. Rosso, J. N. Chazalviel, V. Fleury, and E. Chassaing, *Electrochimica Acta*, **39**, 507 (1994).
60. J. M. Huth, H. L. Swinney, W. D. McCormick, A. Kuhn, and F. Argoul, *Physical Review E*, **51**, 3444 (1995).
61. J. N. Chazalviel, M. Rosso, E. Chassaing, and V. Fleury, *Journal of Electroanalytical Chemistry*, **407**, 61 (1996).
62. V. Fleury, M. Rosso, and J.-N. Chazalviel, *Physical Review A*, **43**, 6908 (1991).
63. A. Kuhn and F. Argoul, *Fractals*, **01**, 451 (1993).
64. A. Kuhn and F. Argoul, *Physical Review E*, **49**, 4298 (1994).
65. A. Kuhn and F. Argoul, *Journal of Electroanalytical Chemistry*, **371**, 93 (1994).
66. K. Brandt, *Solid State Ionics*, **69**, 173 (1994).
67. J.-M. Tarascon and M. Armand, *Nature*, **414**, 359 (2001).
68. D. Aurbach, E. Zinigrad, Y. Cohen, and H. Teller, *Solid State Ionics Proceedings of the Symposium on Materials for Advanced Batteries and Fuel Cells. Organised in conjunction with the International Conference on Materials for Advanced Technologies (ICMAT 2001)*, **148**, 405 (2002).
69. K. Xu, *Chemical Reviews*, **104**, 4303 (2004).
70. M. Armand and J.-M. Tarascon, *Nature*, **451**, 652 (2008).
71. E. J. Cairns and P. Albertus, *Annual Review of Chemical and Biomolecular Engineering*, **1**, 299 (2010).
72. B. Scrosati and J. Garche, *Journal of Power Sources*, **195**, 2419 (2010).
73. V. Etacheri, R. Marom, R. Elazari, G. Salitra, and D. Aurbach, *Energy & Environmental Science*, **4**, 3243 (2011).
74. W. Xu, J. Wang, F. Ding, X. Chen, E. Nasybulin, Y. Zhang, and J.-G. Zhang, *Energy & Environmental Science*, **7**, 513 (2014).
75. Z. Li, J. Huang, B. Yann Liaw, V. Metzler, and J. Zhang, *Journal of Power Sources*, **254**, 168 (2014).
76. Z. Tu, P. Nath, Y. Lu, M. D. Tikekar, and L. A. Archer, *Accounts of Chemical Research*, **48**, 2947 (2015).
77. M. D. Tikekar, S. Choudhury, Z. Tu, and L. A. Archer, *Nature Energy*, **1**, 16114 (2016).
78. J. W. Choi and D. Aurbach, *Nature Reviews Materials*, **1**, 16013 (2016).
79. G. E. Blomgren, *Journal of The Electrochemical Society*, **164**, A5019 (2017).
80. D. Lin, Y. Liu, and Y. Cui, *Nature Nanotechnology*, **12**, 194 (2017).
81. X.-B. Cheng, R. Zhang, C.-Z. Zhao, and Q. Zhang, *Chemical Reviews*, **117**, 10403 (2017).
82. D. Lin, Y. Liu, A. Pei, and Y. Cui, *Nano Research*, **10**, 4003 (2017).
83. P. Albertus, S. Babinec, S. Litzelman, and A. Newman, *Nature Energy*, **3**, 16 (2018).
84. J. Lu, Z. Chen, F. Pan, Y. Cui, and K. Amine, *Electrochemical Energy Reviews*, **1**, 35 (2018).
85. C. Brissot, M. Rosso, J. N. Chazalviel, P. Baudry, and S. Lascaud, *Electrochimica Acta*, **43**, 1569 (1998).
86. C. Brissot, M. Rosso, J. N. Chazalviel, and S. Lascaud, *Journal of Power Sources*, **81–82**, 925 (1999).
87. C. Brissot, M. Rosso, J.-N. Chazalviel, and S. Lascaud, *Journal of The Electrochemical Society*, **146**, 4393 (1999).
88. C. Brissot, M. Rosso, J. N. Chazalviel, and S. Lascaud, *Journal of Power Sources Special Issue: Interfacial Phenomena in Batteries*, **94**, 212 (2001).
89. M. Rosso, T. Gobron, C. Brissot, J. N. Chazalviel, and S. Lascaud, *Journal of Power Sources Proceedings of the 10th International Meeting on Lithium Batteries*, **97–98**, 804 (2001).

90. A. Teyssot, C. Belhomme, R. Bouchet, M. Rosso, S. Lascaud, and M. Armand, *Journal of Electroanalytical Chemistry International Symposium on Material Processing for Nanostructured Devices 2003*, **584**, 70 (2005).
91. M. Rosso, C. Brissot, A. Teyssot, M. Dollé, L. Sannier, J.-M. Tarascon, R. Bouchet, and S. Lascaud, *Electrochimica Acta*, **51**, 5334 (2006).
92. G. M. Stone, S. A. Mullin, A. A. Teran, D. T. Hallinan, A. M. Minor, A. Hexemer, and N. P. Balsara, *Journal of The Electrochemical Society*, **159**, A222 (2012).
93. P. Bai, J. Li, F. R. Brushett, and M. Z. Bazant, *Energy & Environmental Science*, **9**, 3221 (2016).
94. A. Kushima, K. P. So, C. Su, P. Bai, N. Kuriyama, T. Maebashi, Y. Fujiwara, M. Z. Bazant, and J. Li, *Nano Energy*, **32**, 271 (2017).
95. P. Bai, J. Guo, M. Wang, A. Kushima, L. Su, J. Li, F. R. Brushett, and M. Z. Bazant, *Joule* (2018).
96. M. S. Whittingham, *Chemical Reviews*, **104**, 4271 (2004).
97. P. G. Bruce, B. Scrosati, and J.-M. Tarascon, *Angewandte Chemie International Edition*, **47**, 2930 (2008).
98. J. B. Goodenough and Y. Kim, *Chemistry of Materials*, **22**, 587 (2010).
99. J. B. Goodenough and K.-S. Park, *Journal of the American Chemical Society*, **135**, 1167 (2013).
100. J. Vetter, P. Novák, M. R. Wagner, C. Veit, K. C. Möller, J. O. Besenhard, M. Winter, M. Wohlfahrt-Mehrens, C. Vogler, and A. Hammouche, *Journal of Power Sources*, **147**, 269 (2005).
101. M. R. Palacín and A. D. Guibert, *Science*, **351**, 1253292 (2016).
102. N. Williard, W. He, C. Hendricks, and M. Pecht, *Energies*, **6**, 4682 (2013).
103. J. Newman and K. E. Thomas-Alyea, *Electrochemical Systems, 3rd Edition*, 3rd ed. (Wiley-Interscience, Hoboken, N.J, 2004).
104. A. J. Bard and L. R. Faulkner, *Electrochemical Methods: Fundamentals and Applications*, 2nd ed. (Wiley, New York, 2000).
105. I. Rubinstein and L. Shtilman, *Journal of the Chemical Society, Faraday Transactions 2: Molecular and Chemical Physics*, **75**, 231 (1979).
106. H. W. Rösler, F. Maletzki, and E. Staude, *Journal of Membrane Science*, **72**, 171 (1992).
107. J. J. Krol, M. Wessling, and H. Strathmann, *Journal of Membrane Science*, **162**, 145 (1999).
108. J. J. Krol, M. Wessling, and H. Strathmann, *Journal of Membrane Science*, **162**, 155 (1999).
109. I. Rubinshtein, B. Zaltzman, J. Pretz, and C. Linder, *Russian Journal of Electrochemistry*, **38**, 853 (2002).
110. S. M. Rubinstein, G. Manukyan, A. Staicu, I. Rubinstein, B. Zaltzman, R. G. H. Lammertink, F. Mugele, and M. Wessling, *Physical Review Letters*, **101**, 236101 (2008).
111. D. Deng, E. V. Dydek, J.-H. Han, S. Schlumpberger, A. Mani, B. Zaltzman, and M. Z. Bazant, *Langmuir*, **29**, 16167 (2013).
112. S. Schlumpberger, N. B. Lu, M. E. Suss, and M. Z. Bazant, *Environmental Science & Technology Letters*, **2**, 367 (2015).
113. S. Schlumpberger, *Shock electrodialysis for water purification and electrostatic correlations in electrolytes*, Thesis, Massachusetts Institute of Technology (2016).
114. V. V. Nikonenko, N. D. Pismenskaya, E. I. Belova, P. Sistat, P. Huguet, G. Pourcelly, and C. Larchet, *Advances in Colloid and Interface Science*, **160**, 101 (2010).
115. V. V. Nikonenko, A. V. Kovalenko, M. K. Urtenov, N. D. Pismenskaya, J. Han, P. Sistat, and G. Pourcelly, *Desalination Special Issue: Electromembrane Processes for Desalination*, **342**, 85 (2014).
116. H. Strathmann, *Desalination Special Issue to honour the previous editor Miriam Balaban*, **264**, 268 (2010).
117. S. J. Kim, Y.-C. Wang, J. H. Lee, H. Jang, and J. Han, *Physical Review Letters*, **99**, 044501 (2007).
118. G. Yossifon and H.-C. Chang, *Physical Review Letters*, **101**, 254501 (2008).
119. T. A. Zangle, A. Mani, and J. G. Santiago, *Langmuir*, **25**, 3909 (2009).
120. T. A. Zangle, A. Mani, and J. G. Santiago, *Chemical Society Reviews*, **39**, 1014 (2010).
121. T. A. Zangle, A. Mani, and J. G. Santiago, *Analytical Chemistry*, **82**, 3114 (2010).
122. S. Nam, I. Cho, J. Heo, G. Lim, M. Z. Bazant, D. J. Moon, G. Y. Sung, and S. J. Kim, *Physical Review Letters*, **114**, 114501 (2015).
123. J. Schiffbauer, U. Liel, N. Leibowitz, S. Park, and G. Yossifon, *Physical Review E*, **92**, 013001 (2015).
124. S. Sohn, I. Cho, S. Kwon, H. Lee, and S. J. Kim, *Langmuir*, **34**, 7916 (2018).
125. E. V. Dydek, B. Zaltzman, I. Rubinstein, D. S. Deng, A. Mani, and M. Z. Bazant, *Physical Review Letters*, **107**, 118301 (2011).
126. A. Mani, T. A. Zangle, and J. G. Santiago, *Langmuir*, **25**, 3898 (2009).
127. A. Mani and M. Z. Bazant, *Physical Review E*, **84**, 061504 (2011).
128. E. V. Dydek and M. Z. Bazant, *AIChE Journal*, **59**, 3539 (2013).
129. A. Yaroshchuk, E. Zholkovskiy, S. Pogodin, and V. Baulin, *Langmuir*, **27**, 11710 (2011).
130. I. Rubinstein and B. Zaltzman, *Journal of Fluid Mechanics*, **728**, 239 (2013).
131. I. Rubinstein and B. Zaltzman, *Physical Review E*, **62**, 2238 (2000).
132. M. B. Andersen, M. van Soestbergen, A. Mani, H. Bruus, P. M. Biesheuvel, and M. Z. Bazant, *Physical Review Letters*, **109**, 108301 (2012).
133. A. Yaroshchuk, *Advances in Colloid and Interface Science*, **183–184**, 68 (2012).
134. C. P. Nielsen and H. Bruus, *Physical Review E*, **90**, 043020 (2014).
135. R. Aogaki, K. Kitazawa, Y. Kose, and K. Fueki, *Electrochimica Acta*, **25**, 965 (1980).
136. R. Aogaki and T. Makino, *Electrochimica Acta*, **26**, 1509 (1981).
137. R. Aogaki, *Journal of The Electrochemical Society*, **129**, 2442 (1982).
138. R. Aogaki, *Journal of The Electrochemical Society*, **129**, 2447 (1982).
139. R. Aogaki and T. Makino, *Journal of The Electrochemical Society*, **131**, 40 (1984).
140. R. Aogaki and T. Makino, *Journal of The Electrochemical Society*, **131**, 46 (1984).
141. R. Aogaki and T. Makino, *The Journal of Chemical Physics*, **81**, 2154 (1984).
142. R. Aogaki and T. Makino, *The Journal of Chemical Physics*, **81**, 2164 (1984).
143. T. Makino, R. Aogaki, and E. Niki, *The Journal of Chemical Physics*, **81**, 5137 (1984).
144. T. Makino, R. Aogaki, and E. Niki, *The Journal of Chemical Physics*, **81**, 5145 (1984).
145. D. P. Barkey, R. H. Muller, and C. W. Tobias, *Journal of The Electrochemical Society*, **136**, 2199 (1989).
146. D. P. Barkey, R. H. Muller, and C. W. Tobias, *Journal of The Electrochemical Society*, **136**, 2207 (1989).
147. C.-P. Chen and J. Jorne, *Journal of The Electrochemical Society*, **138**, 3305 (1991).
148. M. D. Pritzker and T. Z. Fahidy, *Electrochimica Acta*, **37**, 103 (1992).
149. L.-G. Sundström and F. H. Bark, *Electrochimica Acta*, **40**, 599 (1995).
150. J. Elezgaray, C. Léger, and F. Argoul, *Journal of The Electrochemical Society*, **145**, 2016 (1998).
151. M. Haataja and D. J. Srolovitz, *Physical Review Letters*, **89**, 215509 (2002).
152. M. Haataja, D. J. Srolovitz, and A. B. Bocarsly, *Journal of The Electrochemical Society*, **150**, C699 (2003).
153. M. Haataja, D. J. Srolovitz, and A. B. Bocarsly, *Journal of The Electrochemical Society*, **150**, C708 (2003).
154. G. B. McFadden, S. R. Coriell, T. P. Moffat, D. Josell, D. Wheeler, W. Schwarzacher, and J. Mallett, *Journal of The Electrochemical Society*, **150**, C591 (2003).
155. Q. BuAli, L. E. Johns, and R. Narayanan, *Electrochimica Acta*, **51**, 2881 (2006).
156. C. Monroe and J. Newman, *Journal of The Electrochemical Society*, **151**, A880 (2004).
157. C. Monroe and J. Newman, *Journal of The Electrochemical Society*, **152**, A396 (2005).
158. M. D. Tikekar, L. A. Archer, and D. L. Koch, *Journal of The Electrochemical Society*, **161**, A847 (2014).
159. M. D. Tikekar, L. A. Archer, and D. L. Koch, *Science Advances*, **2**, e1600320 (2016).
160. M. D. Tikekar, G. Li, L. A. Archer, and D. L. Koch, *Journal of The Electrochemical Society*, **165**, A3697 (2018).
161. Z. Ahmad and V. Viswanathan, *Physical Review Letters*, **119**, 056003 (2017).
162. Z. Ahmad and V. Viswanathan, *Physical Review Materials*, **1**, 055403 (2017).
163. P. P. Natsiavas, K. Weinberg, D. Rosato, and M. Ortiz, *Journal of the Mechanics and Physics of Solids*, **95**, 92 (2016).
164. C. P. Nielsen and H. Bruus, *Physical Review E*, **92**, 052310 (2015).
165. J.-N. Chazalviel, *Physical Review A*, **42**, 7355 (1990).
166. V. Fleury, J. N. Chazalviel, M. Rosso, and B. Sapoval, *Journal of Electroanalytical Chemistry and Interfacial Electrochemistry*, **290**, 249 (1990).
167. M. Rosso, J. N. Chazalviel, and E. Chassaing, *Journal of Electroanalytical Chemistry*, **587**, 323 (2006).
168. M. Z. Bazant, *Physical Review E*, **52**, 1903 (1995).
169. J. L. Barton and J. O. Bockris, *Proc. R. Soc. Lond. A*, **268**, 485 (1962).
170. A. R. Despic, J. Diggle, and J. O. Bockris, *Journal of The Electrochemical Society*, **115**, 507 (1968).
171. J. W. Diggle, A. R. Despic, and J. O. Bockris, *Journal of The Electrochemical Society*, **116**, 1503 (1969).
172. C. Monroe and J. Newman, *Journal of The Electrochemical Society*, **150**, A1377 (2003).
173. D. R. Ely and R. E. García, *Journal of The Electrochemical Society*, **160**, A662 (2013).
174. R. Akolkar, *Journal of Power Sources*, **232**, 23 (2013).
175. R. Akolkar, *Journal of Power Sources*, **246**, 84 (2014).
176. P. Verma, P. Maire, and P. Novák, *Electrochimica Acta*, **55**, 6332 (2010).
177. X.-B. Cheng, R. Zhang, C.-Z. Zhao, F. Wei, J.-G. Zhang, and Q. Zhang, *Advanced Science*, **3**, 1500213 (2016).
178. E. Peled and S. Menkin, *Journal of The Electrochemical Society*, **164**, A1703 (2017).
179. A. Wang, S. Kadam, H. Li, S. Shi, and Y. Qi, *npj Computational Materials*, **4**, 15 (2018).
180. J.-H. Han, M. Wang, P. Bai, F. R. Brushett, and M. Z. Bazant, *Scientific Reports*, **6**, 28054 (2016).
181. E. Khoo and M. Z. Bazant, *Journal of Electroanalytical Chemistry*, **811**, 105 (2018).
182. T. R. Ferguson and M. Z. Bazant, *Journal of The Electrochemical Society*, **159**, A1967 (2012).
183. H. J. S. Sand, *Proceedings of the Physical Society of London*, **17**, 496 (1899).
184. M. van Soestbergen, P. M. Biesheuvel, and M. Z. Bazant, *Physical Review E*, **81**, 021503 (2010).
185. M. Bazant, K. Chu, and B. Bayly, *SIAM Journal on Applied Mathematics*, **65**, 1463 (2005).
186. K. Chu and M. Bazant, *SIAM Journal on Applied Mathematics*, **65**, 1485 (2005).
187. W. M. Deen, *Analysis of Transport Phenomena*, 2nd ed. (Oxford University Press, New York, 2011).
188. J. Crank, *Free and Moving Boundary Problems* (Clarendon Press, Oxford Oxfordshire : New York, 1987).
189. R. M. Corless, G. H. Gonnet, D. E. G. Hare, D. J. Jeffrey, and D. E. Knuth, *Advances in Computational Mathematics*, **5**, 329 (1996).
190. R. LeVeque, *Finite Difference Methods for Ordinary and Partial Differential Equations*, Other Titles in Applied Mathematics (Society for Industrial and Applied Mathematics, 2007).
191. J. V. Valério, M. S. Carvalho, and C. Tomei, *Journal of Computational Physics*, **227**, 229 (2007).
192. D. T. Kawano, M. Morzfeld, and F. Ma, *Journal of Sound and Vibration*, **332**, 6829 (2013).
193. D. A. Goussis and A. J. Pearlstein, *Journal of Computational Physics*, **84**, 242 (1989).

194. J. Gary and R. Helgason, *Journal of Computational Physics*, **5**, 169 (1970).
195. G. Peters and J. Wilkinson, *SIAM Journal on Numerical Analysis*, **7**, 479 (1970).
196. M. Rostami and F. Xue, *SIAM Journal on Scientific Computing*, A3344 (2018).
197. F. Xue, "A Solver for the Rightmost Eigenvalues - File Exchange - MATLAB Central".
198. S. Cobeldick, "ColorBrewer: Attractive and Distinctive Colormaps - File Exchange - MATLAB Central".
199. M. Harrower and C. A. Brewer, *The Cartographic Journal*, **40**, 27 (2003).
200. J.-H. Han, E. Khoo, P. Bai, and M. Z. Bazant, *Scientific Reports*, **4**, 7056 (2014).
201. P. T. Hammond, *Advanced Materials*, **16**, 1271 (2004).
202. J. Rumble, ed., *CRC Handbook of Chemistry and Physics, 98th Edition*, 98th ed. (CRC Press, Boca Raton London New York, 2017).
203. R. Krishnan, L. E. Johns, and R. Narayanan, *Electrochimica Acta*, **48**, 1 (2002).
204. E. Mattsson and J. O. Bockris, *Transactions of the Faraday Society*, **55**, 1586 (1959).
205. J. O. Bockris and M. Enyo, *Transactions of the Faraday Society*, **58**, 1187 (1962).
206. O. R. Brown and H. R. Thirsk, *Electrochimica Acta*, **10**, 383 (1965).
207. G. Devaraj, S. Guruviah, and S. K. Seshadri, *Materials Chemistry and Physics*, **25**, 439 (1990).
208. M. S. Chandrasekar and M. Pushpavanam, *Electrochimica Acta*, **53**, 3313 (2008).
209. J. Li, E. Murphy, J. Winnick, and P. A. Kohl, *Journal of Power Sources*, **102**, 302 (2001).
210. B. K. Purushothaman, P. W. Morrison, and U. Landau, *Journal of The Electrochemical Society*, **152**, J33 (2005).
211. B. K. Purushothaman and U. Landau, *Journal of The Electrochemical Society*, **153**, A533 (2006).
212. S. S. Zhang, *Journal of Power Sources*, **161**, 1385 (2006).
213. A. A.-H. Hussein and I. Batarseh, *IEEE Transactions on Vehicular Technology*, **60**, 830 (2011).
214. W. Shen, T. T. Vo, and A. Kapoor, in *2012 7th IEEE Conference on Industrial Electronics and Applications (ICIEA)*, pp. 1567–1572 (2012).
215. F. Savoye, P. Venet, M. Millet, and J. Groot, *IEEE Transactions on Industrial Electronics*, **59**, 3481 (2012).
216. M. Z. Mayers, J. W. Kaminski, and T. F. Miller, *The Journal of Physical Chemistry C*, **116**, 26214 (2012).
217. A. Aryanfar, D. Brooks, B. V. Merinov, W. A. Goddard, A. J. Colussi, and M. R. Hoffmann, *The Journal of Physical Chemistry Letters*, **5**, 1721 (2014).
218. J.-H. Han, R. Muralidhar, R. Waser, and M. Z. Bazant, *Electrochimica Acta*, **222**, 370 (2016).
219. K. Liu, P. Bai, M. Z. Bazant, C.-A. Wang, and J. Li, *Journal of Materials Chemistry A*, **5**, 4300 (2017).
220. P. Bai and M. Z. Bazant, *Nature Communications*, **5**, 3585 (2014).
221. Y. Zeng, R. B. Smith, P. Bai, and M. Z. Bazant, *Journal of Electroanalytical Chemistry*, **735**, 77 (2014).
222. Y. Zeng, P. Bai, R. B. Smith, and M. Z. Bazant, *Journal of Electroanalytical Chemistry*, **748**, 52 (2015).